International Journal of Solids and Structures 328 (2026) 113843

Contents lists available at ScienceDirect

International Journal of Solids and Structures

journal homepage: www.elsevier.com/locate/ijsolstr

Predictive analysis of wrinkling in shrink flanging using conventional versus incremental forming

J.A. López-Fernández [a,*], G. Centeno [b], M.B. Silva [c], C. Vallellano [b]

[a] *Department of Civil, Materials, and Manufacturing Engineering, University of Málaga, C/ Dr. Ortiz Ramos s/n 29071, Málaga, Spain*
[b] *Department of Mechanical and Manufacturing Engineering, University of Seville, Camino de los Descubrimientos s/n 41092, Sevilla, Spain*
[c] *IDMEC, Instituto Superior Técnico, Universidade de Lisboa, Av. Rovisco Pais, 1049-001 Lisboa, Portugal*

ARTICLE INFO

Keywords:
Sheet flanging
Incremental sheet forming
Shrink flanging
Stress–strain analysis
Wrinkling

ABSTRACT

This work presents an experimental and numerical investigation of shrink flanging using Conventional Press Forming (CPF) and Single Point Incremental Forming (SPIF). Tests were carried out on aluminium AA2024-T3 sheets to identify failure modes, process windows, and formability limits under compressive loading. Finite Element simulations were developed for both processes, focusing on the evolution of in-plane stresses at the flange edge. A stress-based wrinkling criterion is stablished, and a process window is defined as a function of flange geometry. Results show that SPIF enhances formability and delays wrinkling compared to CPF. However, while CPF exhibits earlier wrinkling, certain cases allow wrinkle ironing, improving the final surface quality. A numerical criterion is introduced to detect wrinkling based on strain differences between the inner and outer surfaces of the sheet, enabling consistent identification of the wrinkling onset across geometries. A stress-based analysis reveals that the critical compressive stress required to initiate wrinkling is significantly lower in CPF and strongly dependent on flange length. Conversely, SPIF maintains a nearly constant wrinkling limit. Based on these findings, a process window was developed to support the selection of the most suitable forming strategy.

1. Introduction

Thin-walled components are widely used in aerospace and automotive applications due to their high stiffness-to-weight ratio. Among various forming operations, flanging is critical for enhancing structural integrity at the edges of sheet parts. This study addresses shrink flanging of thin-walled aluminium sheets, focusing on the comparative formability using press working and incremental forming (Dewang and Sharma, 2023). Flanges can be classified into various types. Hole flanges are formed in a closed profile, while open flanges are formed in an open profile. Among the operations of open flanging, the straight flanging process involves bending a straight edge, while stretch flanging and shrink flanging produce concave flanges by stretching the material or convex flanges by compressing the material, respectively.

The diversity of sheet metal forming processes allows manufacturers to select the most suitable method based on the complexity of the design, material properties, and production volume. Flanging processes can be performed using various techniques. In the aerospace industry, where production batches are small, rubber forming is commonly used to manufacture these features in structural components. It has been successfully employed for the cold forming of steel (Bałon et al., 2019), aluminium (Tao, et al., 2023), and titanium (Sun et al., 2013); (Chen et al., 2016). Another method utilised for flanging is conventional press forming which is widely used, in conjunction with stamping, in the automotive industry. Given the industrial applications of this process, the research community has devoted considerable effort to the understanding and improvement of the shrink flanging process using rubber forming.

The manufacturing of shrink flanges involves the application of compressive strains to the sheet metal, often through controlled deformation. This compression results in compressive stresses that can eventually cause wrinkling. The primary studies in the literature focus on analysing the process's capabilities, controlling the final geometry, and reducing or even avoiding wrinkling. The pioneering studies on shrink flanging were conducted by Asnafi (1999) and Wang et al. (2001), who analysed the wrinkling of flanges with different geometries obtained using rubber forming. With the aim of predicting the onset of wrinkling Sinke (2012) correlated the flange length with the theoretical strain at the flange edge. Other studies, such as the one by Chen et al. (2011), indicate that wrinkling in shrink flanging through rubber

---

[*] Corresponding author.
E-mail address: alopezf@uma.es (J.A. López-Fernández).

https://doi.org/10.1016/j.ijsolstr.2026.113843
Received 27 June 2025; Received in revised form 20 August 2025; Accepted 9 January 2026
Available online 11 January 2026
0020-7683/© 2026 The Authors. Published by Elsevier Ltd. This is an open access article under the CC BY license (http://creativecommons.org/licenses/by/4.0/).

forming can be prevented by utilising hard rubber and high pressure.

The influence of various factors on shrink flanging, including die radius, flange length, and fillet radius, was investigated by Chen et al. (2015). They analysed the process using different aluminium alloys and proposed a forming method using multiple stages as an effective approach to reduce wrinkling in shrink flanging. Chen et al. (2011) were the first, as far as the authors are aware, to utilise finite elements (FE) for the optimisation of highly curved parts, whereas Chen et al. (2019) employed finite element and experimental studies, proposing an optimised clamping method for the control of wrinkling in sheet metal parts. They identified the height of the flange as the most significant factor influencing wrinkling.

However, the literature remains limited when it comes to flanging with rigid tooling. The pioneering research conducted by Wang et al. (1994) investigated the wrinkling process in shrink flanging by deep drawing, determining the critical strain at wrinkling based on geometric and material variables. The findings demonstrated a high degree of accuracy in predicting wrinkling for the flange radius analysed. In order to predict wrinkling, Wang et al. (2001) proposed an energy approach that was applied to a wide range of curvature radii, from 500 to 2000 mm, that might be extended to a wider range. Analytical models have been employed to predict failure in stretch flanging and shrink flanging, respectively, using conventional press forming and rubber forming (Hu et al., 2003); (Zhang et al., 2003). Furthermore, numerical simulations have proved to be an effective tool for predicting wrinkling. In this context, Draghici (2017) employed FE simulations to predict wrinkling in industrial components with shrink flanges obtained using press forming. More recently, Horton et al. (2020) conducted an experimental study to assess the influence of punch and die radii on wrinkling, applying the findings to an aluminium component.

Although rubber forming and conventional press forming are the most commonly employed flanging processes, incremental sheet forming (ISF) has emerged as a viable alternative to conventional sheet metal forming processes (Emmens et al., Jun. 2010). In ISF, the deformation of sheet metal is performed locally and incrementally using hemispherical tools guided by CNC through a specific path. One variant of this technique is Single Point Incremental Forming (SPIF). This process was first patented by Leszak (1964), and involves the contact of the forming tool on only one side of the sheet metal. The principal advantage of SPIF is the capacity to produce complex parts without the need of expensive forming dies, which significantly reduces costs, especially for the manufacturing of small batches, particularly in the context of prototyping and small-scale production. The SPIF process has been successfully applied to form various metallic materials, including steel (Harfoush et al., 2024), titanium (Thakur and Chauhan, 2024), and aluminium (Choudhary and Mulay, 2024), as well as superalloys (Bishnoi and Chandna, 2024) and bi-metallic sheets (Tayebi and Hashemi, 2024). Additionally, SPIF has been employed to fabricate non-metallic components, mainly using thermoplastic polymers (Zhu et al., 2020); (Rosa-Sainz et al., 2023), but also fibre-reinforced polymers (Emami et al., 2023).

In terms of its industrial applications, SPIF has been successfully used to form a variety of concave and convex parts. This industrial process has also been applied to perform hole flanging in aluminium (Borrego et al., 2016) and steel (Mezher et al., 2021), among other materials. Furthermore, it has been employed to deform other thin-walled geometries, such as tubes (Praveen and Kurra, 2021); (Cristino et al., 2021); (Suntaxi et al., 2021). Although the initial studies applying incremental forming to open flanges were published in the 1990s (Powell and Andrew, 1992), it is only recently that research on shrink flanging by SPIF has definitively emerged (López-Fernández et al., 2024), leading to the study of the factors affecting the process. Another crucial factor in SPIF is the appropriate selection of process parameters, which is essential for achieving a satisfactory result (Gohil and Modi, 2021). Various studies have analysed the influence of the tool geometry (Chen et al., 2019), step down (Basak, 2020), and spindle speed (Ullah et al., 2022). Other researchers have concentrated on predicting the final geometry of parts in terms of thickness (Wang et al., 2022); (Choi and Lee, 2019), as well as on elastic recovery, showing that plastic deformation contributes only marginally to springback (Guzmán et al., 2012).

Numerical simulation has also proven to be a challenging aspect of incremental forming. The complex boundary conditions, such as sheet-tool contact and progressive deformation, make implicit methods less efficient compared to explicit methods due to the time required for computation. In this regard, explicit methods have been successfully applied to simulations, achieving shorter simulation times with fair results. Furthermore, studies have implemented improvements such as adaptive remeshing to reduce simulation time while maintaining accuracy (Voswinckel et al., 2015). On the other hand, recent research employed machine learning techniques to analyse the influence of forming parameters on the final geometry of parts manufactured using ISF (Ostasevicius et al., 2022). In this line, Wang et al. (2022) developed an algorithm capable of predicting the thickness of sheet metal deformed by SPIF, which yielded promising results. Additionally, numerical strategies based on ductile damage models have been employed to improve failure prediction in SPIF (Guzmán et al., 2018) demonstrating its potential to anticipate fracture beyond conventional forming limits.

The analysis of the formability of sheet metal parts obtained using ISF has also been of significant importance. The use of a tool that progressively deforms sheet metal was investigated by Hamedon et al. (2016), demonstrating that gradual punch contact prevents wrinkling in shrink flanging. Recently, Seyyedi et al. (2023) conducted a study comparing the SPIF process with press forming. The researchers concentrated on evaluating the fracture limits in both processes and demonstrated a significant increase in formability with SPIF. Although there are few studies that have analysed the forming of shrink flanges from an incremental perspective, Dewang and Sharma (2023) conducted a comprehensive review of the advancements in shrink flanging in both incremental and conventional forming. Voswinckel et al. (2013) presented a pioneer study analysing the technological capabilities of using ISF for stretch and shrink flanging, highlighting the different material flow behaviour compared to conventional press forming. Given the occurrence of larger geometrical deviations, Voswinckel et al. (2015) designed an adaptive blank holder attached to the tool that reduced the occurrence of undesirable deformations. Additionally, in a combined experimental and numerical analysis, Zhang et al. (2018) demonstrated that higher formability in shrink flanging can be obtained by applying additional meridional tension by concatenating stretch and shrink flanges.

In this scientific and technological context, it can be observed that most previous studies have analysed wrinkling in shrink flanges by studying strains, either analytically, experimentally, or by means of FE. However, Chen et al. (2021)) proposed an alternative approach for incremental forming by spinning that involves analysing wrinkling based on the critical value of circumferential stress achieved in the flange. They applied their study to 360° flanges. Based on this idea, López-Fernández et al. (2023) employed a similar approach to investigate wrinkling in open flanges formed by SPIF, determining the critical values of circumferential stress for wrinkling. The findings of this study demonstrated the viability of manufacturing shrink flanges by SPIF and the potential for accurate wrinkling predictions for small and medium radius flanges. Despite the industrial interest in the manufacture of shrink flanges, no studies analyse the forming limits of open flanges obtained by SPIF, comparing the results with conventional forming processes. Furthermore, most studies in this topic address formability from a strains perspective, which has limitations in predicting wrinkling in SPIF flanges. This shift towards stress-based wrinkling analysis is conceptually aligned with recent mechanics-based formulations of local instability in thin-walled sections, such as the one proposed by Annison and Becque (2025).

For the aforementioned reasons, this research analyses and compares the formability of open compression flanges produced by two different processes, SPIF and CPF, from both experimental and numerical perspectives. The article is divided into six sections. Section 1 contains a state of the art review of the most relevant research on shrink flanges and the technologies commonly used in their manufacture. Section 2 presents the material characterisation in terms of deformations, as well as the tensile mechanical properties and anisotropy necessary for the implementation of the numerical model. Section 3 describes the experimental tests for compression flanges conducted using CPF and SPIF, respectively, while Section 4 details the numerical model designed for both processes. Section 5 presents the results of the study, including the process windows obtained for both methods and a comparative analysis of the two processes in terms of deformations and stresses. Finally, Section 6 offers the conclusions of the work.

2. Material characterization

The material selected for this study is the aluminium alloy AA2024-T3, provided as sheet metal with a thickness of 1.2 mm. This material presents high strength and relatively low formability, and thus, is frequently employed in the aerospace industry for the fabrication of structural components, including wing ribs, longerons and stringers.

The anisotropic properties of the material were analysed by means of tensile tests along the rolling (0°), transverse (90°), and diagonal (45°) directions, respectively. The results obtained are aligned with prior research (Vallellano et al., 2008). Tensile tests were conducted on a universal INSTRON™ 1196 testing machine in accordance with standards (ASTM, 2009) and (ASTM, 2000) to evaluate tensile properties and anisotropy coefficients, respectively. The true stress–strain curve in rolling direction was approximated using the Swift potential law, as represented by Eq. (1). The strain data used to determine the tensile properties was obtained using an axial extensometer model Epsilon, whereas the force data acquisition was conducted using a load cell with a maximum measuring force of 50 kN.

$$\overline{\sigma} = 742.36\left(0.025 + \overline{\varepsilon}^{P}\right)^{0.235} \tag{1}$$

The results, including yield stress, ultimate tensile strength, modulus of elasticity, and Lankford coefficients for each direction are detailed in Table 1. The normal plastic anisotropy ratio was calculated as $\overline{r_\theta} = (r_0 + 2r_{45} + r_{90})/4$ and a Poisson's ratio of 0.33 was assumed.

The formability limits were evaluated through Nakazima tests utilising an Erichsen® model 142–20 universal testing machine and a 100 mm diameter hemispherical punch. To reduce friction, a layer of Vaseline-PTFE-Vaseline was applied. The tests covered a range of five specimen geometries, thereby ensuring a comprehensive analysis of formability across diverse strain paths, from uniaxial to equibiaxial.

The strains evolution during the Nakazima tests was triggered using a 3D Digital Image Correlation (DIC) system, Aramis® version 6.3, with 1.3-megapixel cameras. The identification of the initiation of necking is of crucial importance in the determination of the formability limits, as far as the common methodologies focus on obtaining the FLD by necking. In this study, the Standard ISO 12004–2:2021 (International Standard, 2021) along with a temporal methodology (Martínez-Donaire et al., 2014) were applied to detect the onset of necking. However, none of these methodologies detected the existence of necking prior fracture appearance. As consequence, the formability limit for the studied material is directly represented by the Fracture Forming Limit (FFL). That absence of necking is consistent with previous studies (Vallellano et al., 2008); (López-Fernández et al., 2019); (López-Fernández et al., 2021).

Table 1
Tensile properties in different directions and anisotropy coefficients of AA2024-T3 sheet.

Direction	*σ_Y (MPa)*	*σ_{UTS} (MPa)*	*E (GPa)*	*r_θ*
0°	336	445	69.4	0.76
45°	306	427	67.1	0.95
90°	319	443	68.2	0.54
Average	320	438	68.2	$\overline{r_\theta} = 0.80$

As shown in Fig. 1, the strains paths within the FLD present a constant strain ratio ($\beta = \varepsilon_2/\varepsilon_1$) until fracture. Then, the principal strains at fracture were estimated through thickness measurements in the zone of fracture and the application of volume constancy. This method is suitable for materials that do not show conventional necking before fracture (Centeno et al., 2015).

3. Experimentation

The experimental campaign involved two series of shrink flanging tests, employing two processes: by press forming in a single stroke, and by SPIF in a single stage with hemispherical tool. In both methods, the shrink flanges were formed with a constant flange radius of $R = 45$ mm, which is within the typical industrial flange radius range, for example in aircrafts components.

The undeformed specimens were rectangular sheets obtained by milling with different widths and lengths, as presented in Table 2. The initial lengths of the specimens l_0 ranged from 5 to 25 mm, related to the length range analysed in previous shrink flanging research (Zhang et al., 2018); (Chen et al., 2015). The initial width w_0 of the flanges was defined by multiplying the flange radius by a coefficient ranging from 0.8 to 1.6 in increments of 0.2. Fig. 2 presents a schematic representation of a flange, illustrating the principal geometry parameters. Regarding the flanges performed by SPIF, it must be noted that the actual experimental campaign complements previous research performed by López-Fernández et al. (2023), including additional new tests that were needed in order to enable a comparison of the two flanging methodologies.

The specimen preparation process involved the polishing of the edges of the sheets to eliminate milling marks and the treatment of the top and bottom surfaces with acid to remove surface brightness, a critical step for subsequent optical measurements. Then, the surfaces were electro-etched to produce a pattern of circles of 1 mm diameter spaced 1.5 mm between their centres. Finally, the Argus® Circle Grid Analysis (CGA) system was used to perform surface strain measurements on the deformed flanges. To ensure the consistency of the experimental data, each flanging operation was conducted at least three times using the same geometric parameters and test conditions.

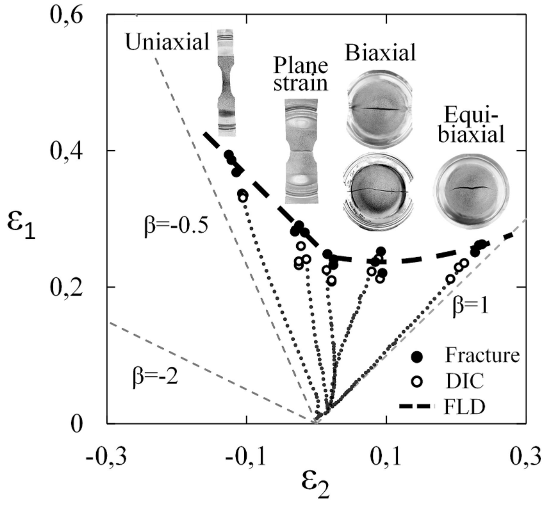

Fig. 1. Forming limit diagram within the principal strains space including, for each specimen, the corresponding strain path, the last point recorded using DIC, and the fracture point.

Table 2
Geometry and process parameters corresponding to the flanges formed by CPF and by SPIF respectively.

	CPF	SPIF
R(mm)	45	
R_{fillet}(mm)	3	
w_0(mm)	36/ 45 / 54 / 63 / 72	
l_0(mm)	5 / 10 / 15 / 20 / 25	
F (mm/min)	60	1000
S (rpm)	–	20
ϕ_{tool}(mm)	–	12
Δ_z(mm)	–	0,4

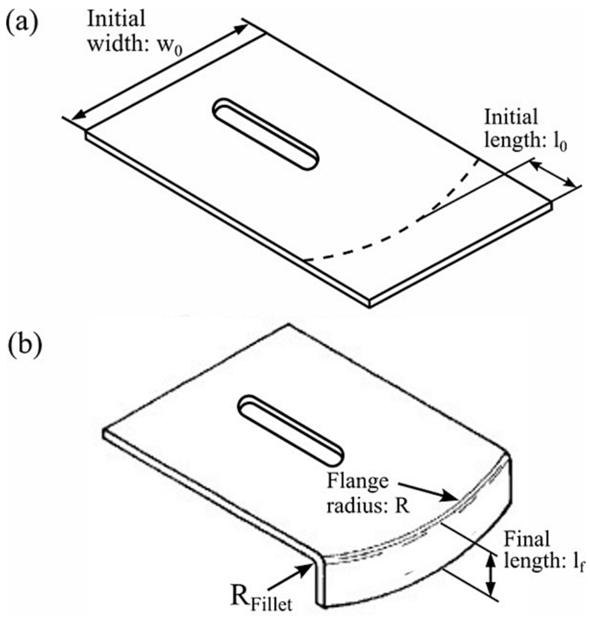

Fig. 2. Schematic representation of a shrink flange depicting the principal geometry parameters: (a) before deformation and (b) after deformation.

3.1. *Flanging by press-working*

Conventional shrink flanging tests were conducted using a Instron SATEC 1200 kN press equipped with a specifically designed setup. The setup comprised a lower concave die and a cylindrical punch attached to the upper platform using a rigid element, see Fig. 3. The vertical movement of the punch is guided by two vertical columns to minimize horizontal displacements. Fig. 3b and Fig. 3c illustrate the CPF process at its initial stage and during the flanging process, respectively.

Prior to each test, the sheet is fixed between the die and the sheet holder, and the punch is lubricated using Lubekrafft® Kl grease with PTFE layers to reduce friction. Then, the punch moves down to form the flange in a continuous vertical displacement at a constant velocity F of 1 mm/s. The test was stopped when the punch stroke reached a depth equal to the sum of the flange initial length l_0 plus the fillet radius R_{fillet} of the die. To prevent the punch from horizontal misalignment during the flanging process, a positioning sheet was placed at the opposite side of the test sheet, as represented in Fig. 3b. This maintains the punch centred with respect to the axis of the die.

Fig. 4 depicts a cross-sectional view of the CPF setup, which illustrates the most representative geometric parameters and dimensions. These include the diameters of the punch and the die, fillet radius R_{fillet} and the gaps between the punch and the die. It is worth noting that the positioning of the sheet had a thickness of 1.4 mm, see Fig. 4.b, whereas the testing sheet was of 1.2 mm thickness, as shown in Fig. 4c. This 0.2 mm gap allows for the expected increase in the flange thickness during material circumferential compression due to shrinking.

3.2. *Flanging by SPIF*

The SPIF experiments were conducted on a three-axis CNC milling machine (EMCO VMC200), utilising the setup depicted in Fig. 5a. The components of this setup included a lower die with a principal convex radius R, a sheet holder, a dynamometer from Kishler®, and a lubrication-cooling system in which compressed cool air was combined with a fine spray of Castrol Iloform® TDN 81 oil directed to the tool–sheet contact region to reduce temperature and friction. Fig. 5b provides a schematic representation of a section view of the setup, which includes the main components and process parameters. The hemispherical SPIF

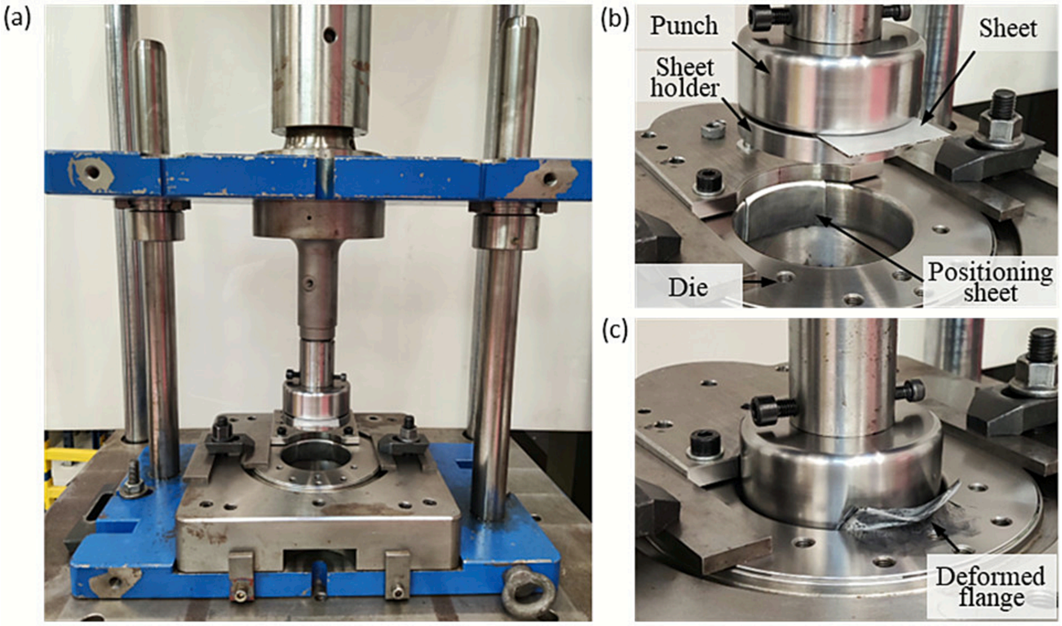

Fig. 3. (a) Vertical press and experimental setup utilised for shrink flanging by CPF. (b) Elements of the shrink flanging setup at the beginning of the CPF process. (c) Elements of the setup during the forming process of a flange with wrinkling.

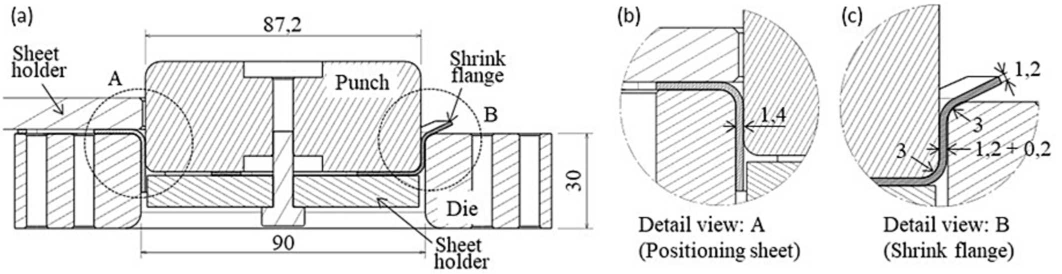

Fig. 4. (a) Section view of the elements of the shrink flanging setup for CPF. (b) Detail view representing the positioning sheet and its thickness. (c) Detail view of the flange depicting the fillet radii, the sheet thickness.

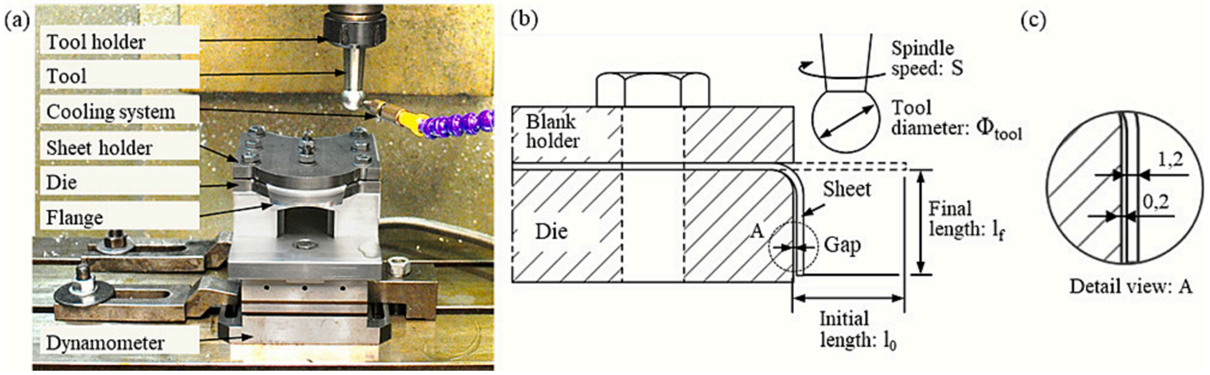

Fig. 5. (a) Setup for shrink flanging by SPIF. (b) Section view representing the elements of the setup and the principal geometric parameters. (c) Detail view depicting the sheet thickness and the gap between the flange and the die.

tool was fabricated from stainless steel and was subjected to a hardening treatment without coating.

Before each incremental test, the aluminium sheet was placed between the die and the sheet holder, with Vaseline and PTFE applied for friction reduction. Subsequently, the tool forms the flange by following programmed arcs in the xy plane and vertical step-downs Δz at the end of each arc. The test ends either when the flange is completely folded, or wrinkles appear. The tool feed speed F was set to 1000 mm/s, with a spindle speed S of 20 rpm, as represented in Table 2. The impact of these parameters on the flanging process was previously investigated (Palomo et al., 2022). These parameters, together with the process parameters for CPF are included in Table 2.

4. Finite element model

A Finite Element Analysis (FEA) was conducted to investigate the stress and strain evolution during both flanging processes. Two finite element models were developed using the commercial explicit dynamics software Ansys LS-Dyna®. The preference for explicit solvers in sheet metal forming research lies in their ability to significantly reduce computational time when compared to implicit FE analysis, especially in incremental sheet forming processes. The simulations were executed on an Intel Xeon CPU E3-1230 v6 (3.50 GHz) processor.

The CPF model is depicted in Fig. 6a, which shows the setup after the onset of wrinkling for a flange with dimensions $w_0 = 45$ mm and $l_0 = 20$ mm. The model incorporates the die, the sheet holder, the forming tool, and the sheet itself, with the forming tool only partially represented to show the flange shape and minor strain contour. It should be noted that, in order to facilitate the analysis of the results and their comparison with the SPIF results, the elements of the CPF model were rotated 180 degrees with respect to their real orientation within the experimental setup. The punch is down, and the die is up to show the flange with the same orientation than in the SPIF simulation represented in Fig. 6b.

The configuration of the SPIF model differs primarily in the forming tool, which is hemispherical (see Fig. 6b for a flange with dimensions $w_0 = 63$ mm and $l_0 = 15$ mm). In this model, the tool emulates the SPIF process, following the tool CNC paths as performed in the SPIF flanging experiments. A particular focus is given to the simulation of the clamping mechanism, which is modelled by applying an initial displacement $z = -0.1$ mm to the sheet-holder.

Both models employed the SHELL163 element type from Ansys for meshing, with a Berlytschko-Tsay formulation and an hourglass control coefficient of 0.01. This element type allows for the simulation of bending processes and the analysis of stress and strain gradients through the use of multiple integration points across the thickness of the sheet. To obtain results from both surfaces of the sheet, five integration points were distributed across the thickness of the sheet. In this regard, Fig. 6a and Fig. 6b illustrate the minor strain contours on the outer surface of the sheet, which is the surface that is not in contact with the tool. The main parameters of the simulation are summarized in Table 3. In both CPF and SPIF simulations, the forming tools were modelled as rigid bodies, which is a standard assumption in sheet metal forming when tool compliance is negligible compared to sheet flexibility. Although studies by Neto et al. (2016) demonstrated that elastic tool deformation can influence pressure distribution in deep drawing processes, such effects are considered minor in the present context. Furthermore, to enhance computational efficiency, the six degrees of freedom per node of the SHELL163, namely three displacements (U_x, U_y, U_z) and three rotations (θ_x, θ_y, θ_z), were selectively restricted, as detailed in Table 4.

The sheet material was modelled using an anisotropic elastic–plastic model with isotropic hardening, based on the Barlat89 (Barlat and Lian, 1989) plasticity criterion. The criterion is represented by equations (2) and (3), where σ_1 and σ_2 represent the in-plane principal stresses, and a, c and h, represented by equation (4), are material constants derived from the Lankford anisotropy coefficients (r_0, r_{45}, and r_{90}). These coefficients were experimentally determined as a result of the material characterisation described in Section 2 and they are listed in Table 1. The yield stress, σ_y, was obtained using a Swift-type curve (Eq. (1),

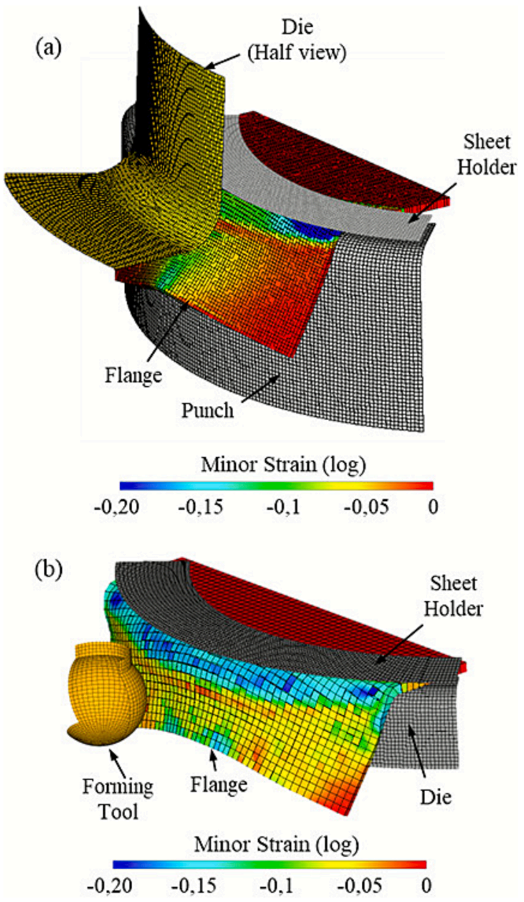

Fig. 6. Finite element models of shrink flanging with minor strain contour evaluated on the outer surface for (a) Conventional Press Forming and (b) Single Point Incremental Forming.

Table 3
Summary of parameters defining the numerical model.

Element	Type	Solid-Shell (SHELL163)
Material	Formulation	Berlytschko-Tsay
	HG control	Stiffness method
	HG coeff.	0.01
	Elem. Size (mm)	0.3–1
	Mat. model	Barlat and Lian (1989)
	Barlat Exp.	m = 8
	Friction coeff.	Press model 0.05 SPIF 0.01
Simulation	Yield Stress	Swift law k = 742.4, n = 0.235
	Mass Scaling	x5
	Time scaling	x1000

Table 4
Element degrees of freedom enabled for each component of the FE models.

Model	**Die**	**Sheet Holder**	**Forming Tool**	**Sheet**
Press Forming	Ø	U_z	U_z	All
SPIF	Ø	U_z	All	All

which was approximated using the true stress–strain curve in the rolling direction. The exponent m was set to 8, in accordance with the recommendations of Logan and Hosford (1980) for the modelling of FCC materials such as aluminium alloys using non-quadratic plasticity criteria.

$$2\sigma_Y^m = a|K_1 + K_2|^m + a|K_1 - K_2|^m + c|2K_2|^m \tag{2}$$

$$K_1 = \frac{\sigma_1 + h\sigma_2}{2} = \frac{(1 + h\alpha)\sigma_1}{2}; K_2 = \sqrt{\left(\frac{\sigma_1 - h\sigma_2}{2}\right)^2} = \sqrt{\left(\frac{(1 - \alpha h)\sigma_1}{2}\right)^2} = \pm\frac{(1 - \alpha h)\sigma_1}{2} \tag{3}$$

$$a = 2 - 2\sqrt{\frac{r_0}{1 + r_0}\cdot\frac{r_{90}}{1 + r_{90}}}; c = 2 - a; h = \sqrt{\frac{r_0}{1 + r_0}\cdot\frac{1 + r_{90}}{r_{90}}} \tag{4}$$

The contact boundary conditions employed a master–slave surface-to-surface approach with Coulomb friction, adopting different friction coefficients (μ) for each model. The optimal friction coefficient for the SPIF model was determined iteratively (López-Fernández et al., 2023) and set to $\mu = 0.01$, starting from $\mu = 0.05$ as suggested by Zhang et al. (2015) and progressively adjusted to achieve the best agreement with experimental strain distribution. The low friction coefficient obtained in this process can be attributed to the efficient continuous lubrication and cooling system employed in the experiments (see cooling system in Fig. 5a). This value is therefore consistent with the expected reduction in tool–sheet friction when using an air–oil spray system, as opposed to the discrete lubrication applied in the CPF setup with Lubekrafft® Kl grease. For the CPF model, a value of $\mu = 0.05$, also taken from the literature (Palomo et al., 2022), was tested by varying the coefficient in increments of ± 0.01 without observing significant changes in the predicted strains or wrinkling behaviour; higher values led to unrealistic deviations from the experiments. This value showed strain evolutions very consistent with those measured experimentally.

In numerical modelling, explicit dynamical integration schemes permit the use of two techniques to reduce computational time, i.e. time scaling and mass scaling. These techniques require a careful consideration of the influence that alterations in speed and density may have on the simulation, as they may lead to convergence issues and non-realistic results. In both models, mass and time scale factors of $ms = 5$ and $ts = 1000$ were employed, respectively, which resulted in a considerable reduction in calculation time from days to hours that was particularly notable in the FE model of SPIF. The value $ms = 5$ was chosen after testing values up to 10, as higher values alter the dynamic response and led to instabilities, particularly at the flange edges. In SPIF simulations, time scaling is especially sensitive during initial tool–sheet contact, which occurs repeatedly at the beginning of each circular arc. To avoid the undesired effects that high time scaling can cause in these contact events, the general value $ts = 1000$ was reduced to $ts = 10$ only during these critical moments. This approach preserved contact stability while maintaining the overall computational time reduction, which was particularly notable in the FE model of SPIF. In addition, the SPIF tool trajectory was implemented as displacement boundary conditions by defining three vectors with the x, y, and z coordinates of the experimental path, discretised every 0.1 mm. The corresponding time vector was obtained by dividing the distance between consecutive points by the experimental feed speed ($F = 1000\,mm/s$). After applying the time scaling factor (ts = 1000), the scaled time vector was used to prescribe the tool motion.

In order to determine the element size, a sensitivity analysis was carried out for both the press-forming and SPIF models in terms of principal strains. This demonstrated an overall convergence for element sizes of 1 mm. The comparison with experimental CGA measurements, taken at the centre of the flange edge and evaluated at a distance of 1 mm from the edge to minimise uncertainty, showed no significant variation in predicted strains for further refinements below this size. As an illustration, the simulation time for a CPF model with 2500 elements was approximately 45 min, whereas the simulation time for the equivalent SPIF model was 13 h.

5. Results

Section 5 presents the results from the investigation on shrink flanging using Conventional Press Forming (CPF) and Single Point Incremental Forming (SPIF). These results are organised into five main subsections: Section 5.1 details the primary failure modes observed in both CPF and SPIF processes. It includes a classification of these modes and provides a comparative assessment of how geometry parameters influence formability, resulting in distinct process windows. Section 5.2 builds upon the failure mode classification to establish the process windows for CPF and SPIF. This subsection provides a detailed comparison of the different results obtained, empathising the impact of flange dimensions on the success of the forming processes. Section 5.3 explores the limits of formability for both CPF and SPIF, providing a comprehensive understanding of the flange behaviour and the wrinkling limit under different forming scenarios. Section 5.4 presents a numerical criterion for the determination of wrinkling based on principal strains and section 5.5 analyses comparatively the formability of the two flanging processes analysed, CPF and SPIF.

5.1. Modes of failure

The experimental campaign involved 25 flanges with varying initial widths and lengths, manufactured using CPF and SPIF, respectively. The values of the different process parameters were previously outlined in Section 3. A total of 50 different flanges were replicated at least three times to ensure consistency in the results. The primary modes of failure were identified, and process windows for both processes were obtained.

Fig. 7 illustrates a classification of the different failure and no-failure cases obtained for conventional press working with images of representative flanges. On the one hand, Fig. 7a and 7b display two successful flanges achieved using CPF. As observed, the flange surfaces are smooth, with no signs of sheet instability or discontinuities. On the other hand, the primary mode of failure observed is wrinkling (w). This failure mode occurs when, at any point during the experiment, wrinkles appear, regardless of whether the final part presents them or not. Based on the experimental evidence, a flanged component with wrinkling may develop one wrinkle (1w*) or two wrinkles (2w*) respectively, as depicted in Fig. 7b and 7c. The asterisk '*' indicates that the number of wrinkles was evaluated at the onset of wrinkling. From a technological perspective, the flanges should be completely formed; thus, these examples are used for illustrative purposes of an intermediate step in the forming sequence. Once wrinkling begins in CPF, the displacement of the stroke can continue, further forming the flange beyond the onset of wrinkling. In such cases, the wrinkles are ironed out, and these flanges are ultimately successful (S), as noted in Fig. 7e and 7f. However, for certain flange widths and lengths, the wrinkles are too pronounced to be fully ironed out, and the friction with the stroke induces a fracture (F), sometimes partial as in Fig. 7g, and occasionally resulting in a complete split of the flange as shown in Fig. 7h.

Regarding the SPIF process, the results obtained have been classified into three categories. In this process, the flanges are considered successful using the same criterion that was employed for CPF. These flanges have a smooth flange wall and do not exhibit wrinkling, as shown in Fig. 8a. In contrast, flanges with wrinkling exhibit different results in SPIF compared to CPF. In CPF, the narrow gap between the stroke and the die allows for the ironing of the sheet. However, in SPIF, there is no lower die, and the forming tool deforms the sheet locally. Therefore, after wrinkling initiates, they cannot be reduced or suppressed by ironing. In this regard, the modes of failure observed in SPIF are wrinkling and incipient wrinkling respectively. To this regard, incipient wrinkling (iw) is defined as the initial formation of wrinkles that do not develop further due to the absence of conditions conducive to the formation of larger wrinkles. In this instance, the process can continue, and the flange can be formed, although with some deformations, as illustrated in Fig. 8b. The alternative is “simple”

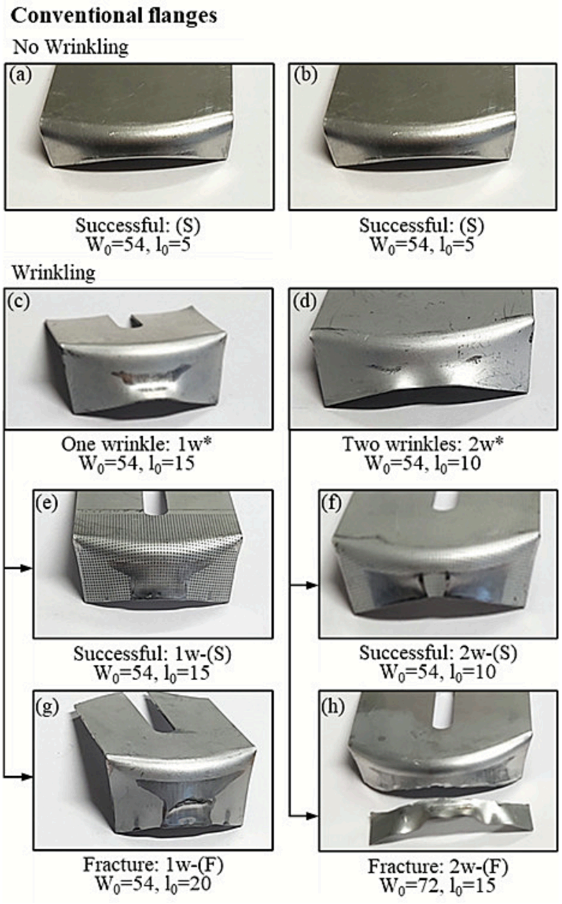

Fig. 7. Selection of flanges obtained by Conventional Press Forming which represent the different cases obtained from the experimental tests. (a-b) Successful flanges without wrinkling. (c) Flange with one wrinkle. (d) Flange with two wrinkles (e) Flange with one wrinkle, after ironing. (f) Flange with two wrinkles, after ironing. (g) Flange with one wrinkle that resulted in fracture during the ironing (h) Flange with two wrinkles that resulted in fracture during the ironing.

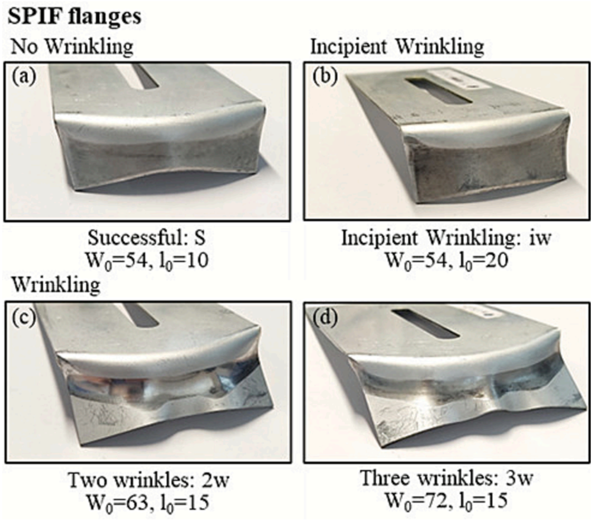

Fig. 8. Selection of flanges obtained by SPIF which represent the different cases obtained from the experiments. (a) Successful flange without wrinkling. (b) Flange with incipient wrinkling. (c) Flange with two wrinkles. (d) Flange with three wrinkles.

wrinkling, whereby wrinkles appear and increase in size as the process progresses. In this case, it is imperative to terminate the process to prevent any damage to the forming tool. Two examples of flanges exhibiting this mode of failure are illustrated in Fig. 8c and 8d, with two and three wrinkles, respectively.

5.2. Process windows

Once the potential failure modes of CPF and SPIF had been identified and classified, the process windows for both methods were established. Table 5 presents a classification of the flanges based on the forming process, flange width, and flange length, indicating the type of result obtained after the forming process. The terminology used in the table is consistent with the specifications provided in Section 5.1. The table details the number of wrinkles observed in each case (1w, 2w), the type of wrinkle (w, iw), and the outcome of the flanging process, categorised as either successful (S) or fracture (F).

From the data presented in Table 5, several conclusions can be drawn. Firstly, it can be observed that only very short flanges of 5 mm in length l_0 were successful in the case of CPF. Given that the fillet radius R_{fillet} is 3 mm, the straight length of these flanges is approximately 2 mm. Without considering those very short flanges, it can be concluded that in CPF wrinkles occur even in very short flanges regardless of the width w_0. However, for SPIF, the zone with wrinkle-free flanges is significantly larger, corresponding to all flanges of $l_0 \leq 10$ mm and several flanges of $l_0 \leq 15$ mm.

The zone of wrinkle-free flanges observed in SPIF indicates what could be logically expected, i.e that increasing the width of the flanges w_0 favours the appearance of wrinkles, whereas decreasing the length of the flanges l_0 prevents them.

Although the existence of wrinkling in a formed flange has been already identified, it is necessary to determine whether such flanges can be considered acceptable from an industrial perspective. In order to carry it out, it is essential to identify the parameters that determine the quality of the flanges in each case. With regard to CPF, the yellow region corresponds to flanges with wrinkles that can be reduced through ironing. In contrast, the red area shows flanges with wrinkles that lead to fracture. It can be observed that there is a correlation between the number of wrinkles (1w or 2w) and the geometrical parameters w_0 and l_0. Specifically, only for the shortest flanges ($l_0 \leq 15$ mm) does wrinkling with two wrinkles occur. However, no correlation was observed between the number of wrinkles and the possibility of ironing the flange without causing fracture. The results indicate that flanges with high values of both w_0 and l_0 cannot be ironed and always result in fracture after wrinkling. Oppositely, in the case of SPIF, there exists a clear relationship between flange width and the type of wrinkles. Specifically, in flanges with $w_0 < 63$ mm, if wrinkles appeared they were incipient, whereas for larger values of w_0 wrinkling was always observed.

In conclusion, several observations can be made regarding the process windows of CPF and SPIF. Firstly, an increased formability of the material due to SPIF is observed, allowing for wrinkle-free flanges at higher values of w_0 and l_0 compared to CPF, as shown by the green shaded areas in Table 5. However, it is important to notice that there is a broad range of w_0 and l_0 values in CPF where ironing without fracture occurs. In this region, represented in yellow, although wrinkling occurs, ironing produces a flange with higher quality in terms of shape and roughness compared to the same flange obtained via SPIF. With regard to this, the most suitable manufacturing process for the analysed flanges has been represented in Table 6. It is important to point out that this analysis does not consider other factors, such as tooling cost savings for short series or manufacturing time, in which case the optimum process could be different.

Table 5

Process window for $R = 45mm$. The nomenclature corresponds to S (Successful), 1w (one wrinkle), 2w (two wrinkles), F (fracture) and iw (incipient wrinkling). Green corresponds to successful flanges without wrinkling. Yellow represents flanges which resulted successful after ironing or successful flanges with incipient wrinkling. Red corresponds to failed flanges either by fracture or by wrinkling respectively. The bold-underlined cases are analysed in section 5.

		w_0 [mm]				
	l_o [mm]	36	45	54	63	72
CPF	5	S	S	S	S	S
	10	1w-(S)	2w-(S)	**2w-(S)**	2-w(S)	2-w(S)
	15	1w-(S)	1w(S)	1w-(S)	2w-(F)	2w-(F)
	20	**1w-(S)**	**1w-(S)**	1w-(F)	1w-(F)	1w-(F)
	25	1w-(S)	1w-(S)	1w-(F)	1w-(F)	1w-(F)
SPIF	5	S	S	**S**	S	S
	10	S	S	**S**	S	S
	15	S	S	S	2w	2w
	20	S	**iw-(S)**	iw-(S)	2w	2w
	25	iw-(S)	iw-(S)	iw-(S)	2w	2w

Table 6

Overall process window for $R = 45mm$ representing the optimal flanging process (CPF or SPIF) attending to the flange shape. Green corresponds to successful flanges without wrinkling. Yellow represents flanges which resulted successful after ironing or successful flanges with incipient wrinkling. Red color corresponds to the flanges that cannot be successfully obtained by either process.

		w_0 [mm]				
	l_o [mm]	36	45	54	63	72
CPF	5	CPF	CPF	CPF	CPF	CPF
	10	CPF	CPF	CPF	CPF	CPF
	15	CPF	CPF	CPF	🟥	🟥
	20	CPF	CPF	SPIF	🟥	🟥
	25	CPF	CPF	SPIF	🟥	🟥

5.3. Strain analysis and numerical validation

This section examines the strain distribution within the FLD for different flanges formed using SPIF and CPF processes. Subsection 5.3.1 compares strains for various representative flanges in order to understand the differences in forming behaviours and wrinkling tendencies between SPIF and CPF. Subsection 5.3.2 presents the validation of the FE model by comparing numerical and experimental strain results for different flanges. Finally, Subsection 5.3.3 examines the temporal evolution of stresses and strains to determine the conditions that cause wrinkling, thereby providing a comprehensive wrinkling analysis for both CPF and SPIF processes.

5.3.1. Strain distribution within the FLD

In Section 5.2, it has been demonstrated that flanges with identical initial geometry behave differently depending on the manufacturing process employed. It was observed that in SPIF, longer and wider flanges could typically be achieved without wrinkles compared to the conventional process. Additionally, it was noticed that in CPF, although wrinkles appear in nearly all cases, they can sometimes be removed by continuing the forming process, resulting in the flange “ironing”. To better understand the factors influencing forming in both processes, a comparative analysis was conducted focusing on strains for various representative flanges produced by both methods. These flanges correspond to the cases highlighted in bold and underlined in Table 5.

For the initial analysis, a flange with $w_0 = 36$ mm and $l_0 = 20$ mm was selected. Using CPF, this flange initially presents a wrinkle which is subsequently ironed out, whereas in SPIF, the same flange is successfully formed to the end without the appearance of wrinkles. The strain analysis obtained from the strain measurements with Argus presented in Fig. 9 shows the major and minor strain contours for both flanges evaluated on the inner face, whereas Fig. 10 depicts the strain points represented on the principal strains diagram. Since the onset of wrinkling was always observed in the centre of the flange, which corresponds to the section illustrated in Fig. 9c, the central section of the flange has been analysed, as represented in Fig. 10.

From Fig. 9, some similarities between both flanges can be observed. Firstly, the maximum major strain values are localised in the central area of the flange, due to the stretching in the radial direction caused by friction with the tool. Secondly, as represented in Fig. 9c and 9d, the area with highest compression is the corner of the flange. Considering that the strain measurements were performed on the inner surface, those high levels of compression are caused by bending. Consequently, wrinkling occurs within the centre of the flange edge, which has the highest compression levels for both processes without considering the mentioned bending effect.

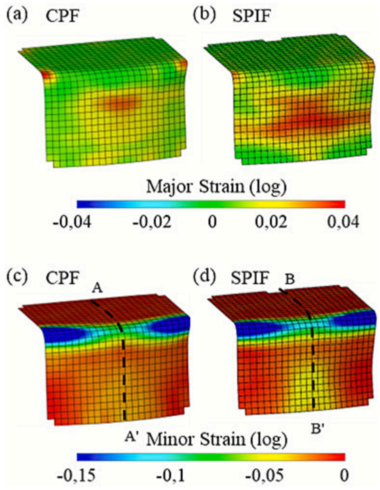

Fig. 9. Principal strains contours of two flanges of $w_0 = 36$ mm and $l_0 = 20$ mm evaluated on their inner surface: a flange with wrinkles subsequently ironed obtained by CPF and a successful flange obtained by SPIF, respectively. (a) Major strain contour in CPF. (b) Major strain contour in SPIF. (c) Minor strain contour in CPF. (d) Minor strain contour in SPIF.

Regarding the representation of strains in the FLD, although the strain values are different for both processes, it can be seen that all points lie in the second quadrant and both central sections have similar shape. The area of the section subjected exclusively to compression is the bending area, while the area with higher major strain corresponds to the centre of the flange. It is important to note that the ends of the sections depicted in Fig. 10 represent the last point measured using CGA, which is located 1 mm from the flange edge.

Despite the aforementioned similarities, differences in strain can be observed depending on the forming process used. Specifically, the edge

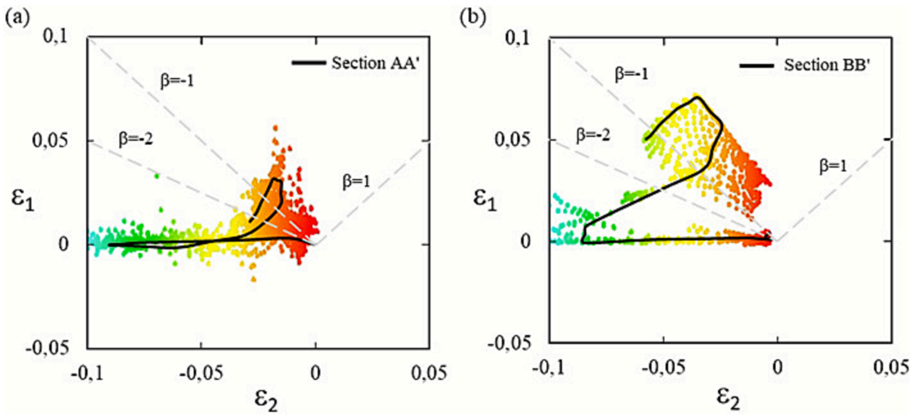

Fig. 10. Strain distribution within the FLD with central section of two flanges of $w_0 = 36$ mm and $l_0 = 20$ mm. (a) A flange with wrinkles subsequently ironed obtained by CPF. (b) A successful flange obtained by SPIF.

of the flange obtained by SPIF (see Fig. 9d) is more compressed than the flange obtained by CPF. This should theoretically favour wrinkling in SPIF compared to CPF. However, incremental forming causes a radial stretching of the flange, which produces higher major strains than using the CPF process, as illustrated in Fig. 9a and Fig. 9b. Additionally, the end of the section is closer to the theoretical wrinkling level $\beta = -2$ in the flange formed by CPF. Notably, points located below the $\beta = -2$ line are expected to develop wrinkling. In this case, the end of the section in the CPF flange lies closer to this limit than in SPIF.Overall, these results explain why for equal initial geometry, some flanges formed by SPIF do not have wrinkles, whereas the flanges formed by CPF may wrinkle.

In addition to wrinkling, the FLD in Fig. 10 allows assessing local thickness changes, since thickness strain is given by $\varepsilon_3 = -(\varepsilon_1 + \varepsilon_2)$. Points above the $\beta = -1$ line indicate thinning, while points below it indicate thickening. For this case, both CPF and SPIF show areas of thinning and thickening. However, SPIF exhibits a greater proportion of points above $\beta = -1$, suggesting higher overall thinning, and almost no thickening at the flange edge. In contrast, CPF shows marked edge thickening, with the extreme point of the section even below $\beta = -2$.

The same analysis described above is shown in Figs. 11 and 12 for a flange with $w_0 = 45$ mm and $l_0 = 20$ mm. The flange formed by CPF had wrinkling followed by ironing, whereas the flange formed by SPIF had incipient wrinkling. In this case, the trend in terms of major and minor strain distribution is similar to the flange presented in Fig. 9, i.e. the highest major strain levels are in the centre of the flange and the maximum compression occurs at the centre of the edge. However, the major strains for both CPF and for SPIF, as shown in Fig. 11a and Fig. 11b are higher than in successful flanges (see Fig. 9a and Fig. 9b), indicating more stretching of the flange in longitudinal direction, and the levels of minor strains at the edge are lower, as shown in Fig. 11c and 11d. This increase of the edge compression in the circumferential direction is probably what causes the wrinkling. In these regards, a similar trend is observed comparatively in the FLDs represented in Figs. 10 and 12.

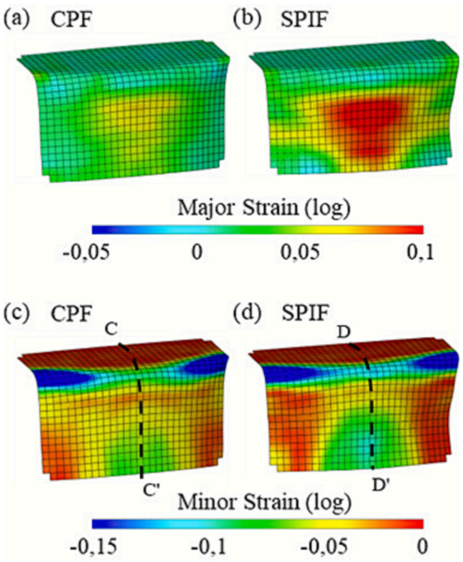

Fig. 11. Principal strains contours of two flanges of $w_0 = 45$ mm and $l_0 = 20$ mm evaluated on their inner surface: a flange with wrinkles subsequently ironed obtained by CPF and a flange with incipient wrinkling obtained by SPIF, respectively. (a) Major strain contour in CPF. (b) Major strain contour in SPIF. (c) Minor strain contour in CPF. (d) Minor strain contour in SPIF.

As in the previous case, both processes produce regions of thinning and thickening. SPIF results in higher global thinning and only a slight edge thickening (edge point just below $\beta = -1$), whereas CPF presents less overall thinning and more pronounced thickening at the edge, with the extreme point below $\beta = -2$.

Finally, Figs. 13 and 14 analyse three flanges with $w_0 = 54$ mm and $l_0 = 10$ mm. First, a case of wrinkling and ironing performed by CPF is examined. To understand the strain conditions of this failure mode, the flange is analysed at two different stages of the process: at the beginning of wrinkling (Figs. 13a, 13d, and 14a) and at the end of the process after ironing (Figs. 13b, 13e, and 14b). Secondly, the same flange formed by SPIF is analysed in Figs. 13c, 13f, and 14c.

Performing a critical analysis of Fig. 13, several aspects must be highlighted. Firstly, the flange formed by CPF analysed at the onset of wrinkling shows two zones with high levels of major strain represented in red. Additionally, this flange also shows high compression levels at the edge corresponding to the onset of the two wrinkles. These two wrinkles can be clearly identified in Fig. 7d. As the forming process continues and ironing occurs, the flange is pressed between the die and the tool, and the wrinkles are gradually reduced and removed. The results presented in figure 13b show that the ironing process increases the area of high major strains and extend it towards the edge of the flange due to the flange stretching. Similarly, the area with high compression shown in Fig. 13d is more extensive and with higher values in the ironed flange (Fig. 13e). Additionally, it can be observed in the principal strain diagram represented in Fig. 14a that the central section is curved at its end at the onset of wrinkling with lower minor strain levels, whereas the strain distribution after the ironing process (Fig. 14b) shows higher values of major strains and lower minor strains.

On the other hand, in the flange formed by SPIF (Fig. 13c and 13f) the major strains are more homogeneously distributed, and the levels are lower compared to the flange obtained by CPF analysed at the wrinkling onset. It is important to note that despite the higher and

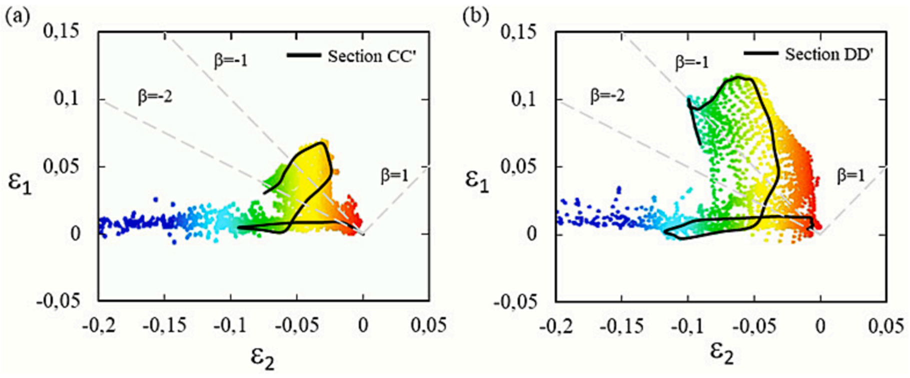

Fig. 12. Strain distribution within the FLD with central section of two flanges of $w_0 = 45$ mm and $l_0 = 20$ mm. (a) A flange with wrinkles subsequently ironed obtained by CPF. (b) A flange with incipient wrinkling obtained by SPIF.

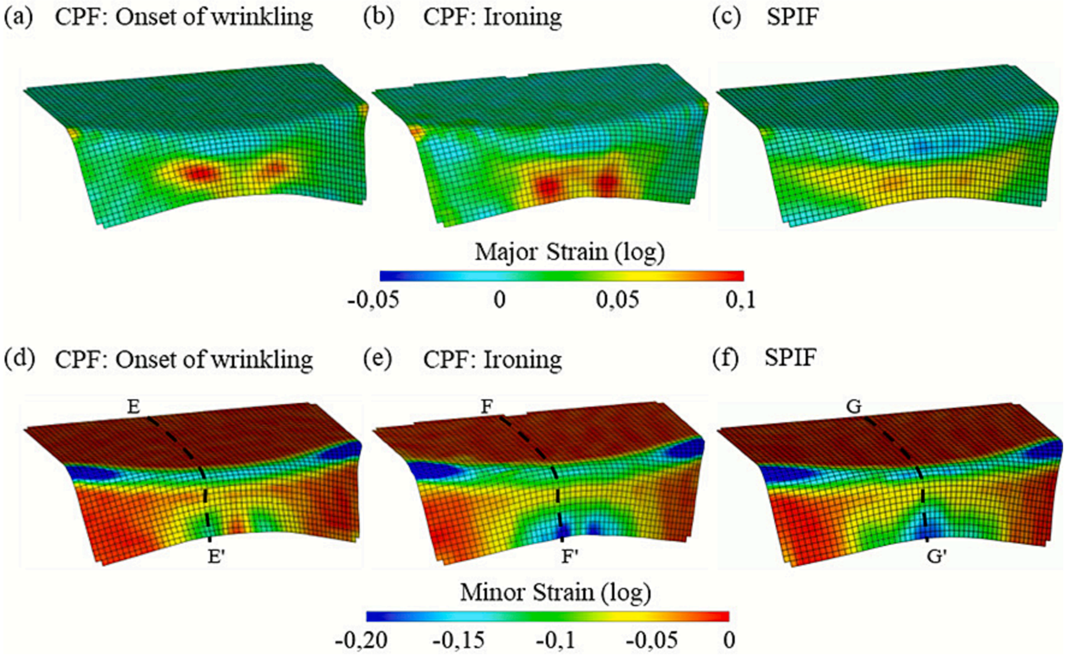

Fig. 13. Principal strains contours of two flanges of $w_0 = 54$ mm and $l_0 = 10$ mm evaluated on their inner surface: a flange with wrinkling and ironing obtained by CPF, and a successful flange obtained by SPIF, respectively. (a) Major strain contour pre-ironing (CPF). (b) Major strain contour post-ironing (CPF). (c) Major strain contour (SPIF). (d) Minor strain contour pre-ironing (CPF). (e) Minor strain contour post-ironing (CPF). (f) Minor strain contour (SPIF).

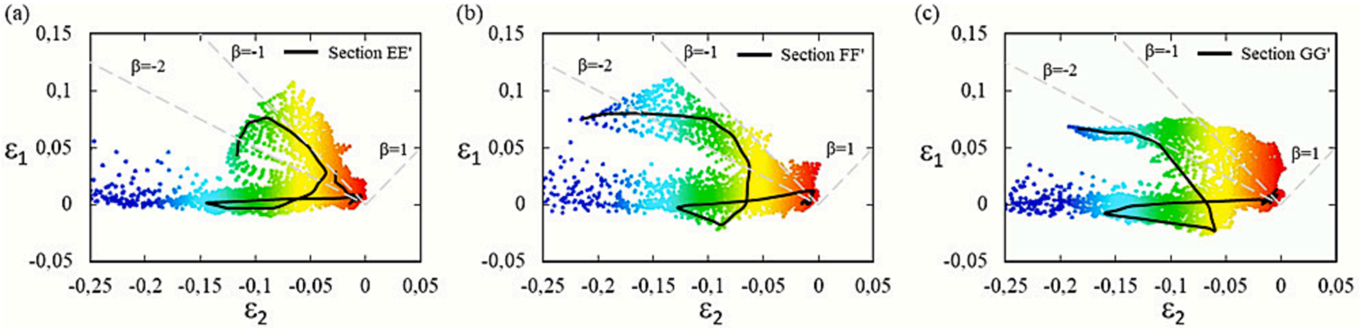

Fig. 14. Strain distribution within the FLD with central section of two flanges of $w_0 = 54$ mm and $l_0 = 10$ mm. (a) A flange with wrinkles subsequently ironed obtained by CPF in the instant prior the ironing. (b) The same flange after the ironing process. (c) A successful flange obtained by SPIF.

localised compressions at the centre of the edge, this flange does not have wrinkles, as shown in Fig. 8a, indicating that wrinkling occurs at different strain levels depending on the chosen process. Finally, the analysis of the central sections performed in Fig. 14 shows that, in terms of principal strains, the flange obtained by SPIF is much more similar to the flange obtained using CPF after ironing (Fig. 12b) than the same flange at the onset of wrinkling (Fig. 13a).

For both fully formed flanges depicted in Fig. 14b a and 14c, similar edge thickening levels are observed (section below $\beta = -2$). However, SPIF shows a larger region with thinning (points above $\beta = -1$), whereas CPF ironing produces thickening over most of the flange.

In summary, the strain analysis shows that both processes produce different levels of principal strains. Generally, the SPIF process causes higher major strain levels and lower minor strain levels than CPF. Both CPF and SPIF flanges show areas of thinning and thickening, but SPIF tends to produce more overall thinning and less edge thickening than CPF. Although flanges obtained by SPIF present higher compression, they are less susceptible to wrinkling for a given initial flange geometry. This result demonstrates an increased formability and the ability of SPIF to delay or even supress wrinkling, likely due to the localised and incremental deformation. Additionally, in line with observations by López-Fernández et al. (López-Fernández et al., 2023) for flanges formed by SPIF, it has been shown that strain levels are not a good method for predicting wrinkling, as they do not show a clear trend in wrinkling occurrence.

5.3.2. Strain validation of the FE model

With the aim of further studying the wrinkling process in the flanges and comparing the results with those obtained for SPIF (López-Fernández et al., 2023) a numerical model has been created to simulate the forming of flanges using CPF. This model has been validated in terms of principal strains using the three representative cases previously analysed in terms of deformations.

Fig. 15 shows, the numerical and experimental strains evaluated in the central section of the flanges highlighted in bold and underlined in Table 5 for the CPF process. The flange analysed in Fig. 15a does not have wrinkles, whereas the flanges of Fig. 15b and Fig. 15c correspond to cases of wrinkling and successful ironing, respectively. In both the numerical and experimental cases, the sections have been evaluated at the end of the process. It can be observed that for the three cases studied, and considering that it is an explicit model, the numerical section agrees fairly with the experimental strains.

Additionally, the real shape resulted from the experiments (Fig. 16a and 16c), the minor strain contours obtained using CGA (Fig. 16b and 16d) and the corresponding FE results of the flange with $w_0 = 54$ mm and $l_0 = 10$ mm have been compared. It can be seen that the numerical and experimental minor strain contours at the onset of wrinkling and at the end of the ironing process, respectively, are very similar, and in both cases the model represents accurately the localised compression strains at the edge of the flange. Furthermore, the shape of both flanges obtained through FEA coincides with the shape of the actual flanges represented in Fig. 16a and 16c.

Similarly, Fig. 17 shows the numerical strain contour of a flange with $w_0 = 72$ mm and $l_0 = 10$ mm. In this case, it has been chosen a flange with wrinkling that is representative due to its asymmetric wrinkles. From the analysis of this flange, it can be observed that the model reproduces not only the strain levels but also the number and shape of the wrinkles. It should be noted that, given the symmetry of the process, in this case the wrinkles have appeared on opposite locations in the numerical and experimental processes, as seen in Fig. 17c and 17d.

Following the results presented, it can be concluded that the numerical model has been satisfactorily validated and can be used for the prediction of strains in oncoming sections.

5.3.3. Wrinkling analysis in terms of principal strains

The previous analyses allowed for the examination of deformations at a given moment. However, to determine the conditions that cause wrinkling, it is necessary to analyse the temporal evolution of stresses and strains. Following the approach of Magrinho et al. (2018), the onset of wrinkling has been studied in terms of deformations in the FLD. To this end, the evolution of principal strains at the critical wrinkling point, which is the centre of the flange edge, have been analysed for three representative flanges obtained through CPF and SPIF, respectively.

The first case is a flange with $w_0 = 54$ mm and $l_0 = 5$ mm, selected to analyse a wrinkle-free (successful) flange in both SPIF and CPF. The second case corresponds to a flange with $w_0 = 54$ mm and $l_0 = 10$ mm, which has been previously analysed using CGA. This flange presents two wrinkles, which are later ironed, when it is formed using CPF, whereas it is successful using SPIF. Lastly, the third case corresponds to a flange with $w_0 = 45$ mm and $l_0 = 20$ mm that presents one wrinkle followed by ironing when it is formed by CPF and incipient wrinkling when it is formed by SPIF.

Fig. 18 shows the numerical evolution of strains for the three flanges manufactured using CPF, evaluated on both surfaces of the sheet (outer and inner). In Fig. 18a, which corresponds to the flange without wrinkles, the evolution of the critical point, located at the centre of the edge, follows a proportional strain path with the same strain ratio β for both surfaces. However, due to the flange curvature, the strain at the end of the CPF process for the two surfaces is different. The inner surface is more compressed, as it is on the concave side of the flange. On the other hand, Fig. 18b corresponds to a flange with two wrinkles where the critical point is more compressed on the outer surface (concave) than on the inner surface (convex). For this flange, the inner and outer surfaces have quite different behaviour. On one hand, the strain path corresponding to the outer surface follows a nearly linear strain path before and after the onset of wrinkling. On the other hand, the evolution of the inner surface deviates towards a less compressed zone of the FLD when wrinkling occurs and shifts back to the left during ironing. Finally, Fig. 18c shows the evolution of the flange with one wrinkle that was previously analysed in Fig. 13. In that flange, the inner surface corresponds to the concave area of the wrinkle and follows an almost constant strain path, even after wrinkling. In contrast, the evolution of the outer surface has four segments. The first segment, depicted using a continuous black line, represents the strain path up to the wrinkling onset. This

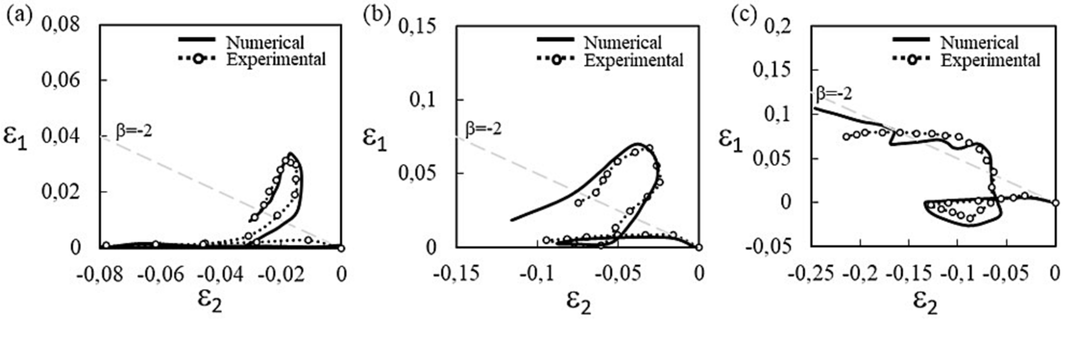

Fig. 15. Strain validation of the CPF numerical model using experimental and numerical critical sections at flange centre corresponding to the following flanges: (a) a successful flange with initial width $w_0 = 36$ mm and initial length $l_0 = 20$ mm, (b) a flange with wrinkling with initial width $w_0 = 45$ mm and initial length $l_0 = 20$ mm, and (c) a flange with wrinkling and ironing with initial width $w_0 = 54$ mm and initial length $l_0 = 10$ mm.

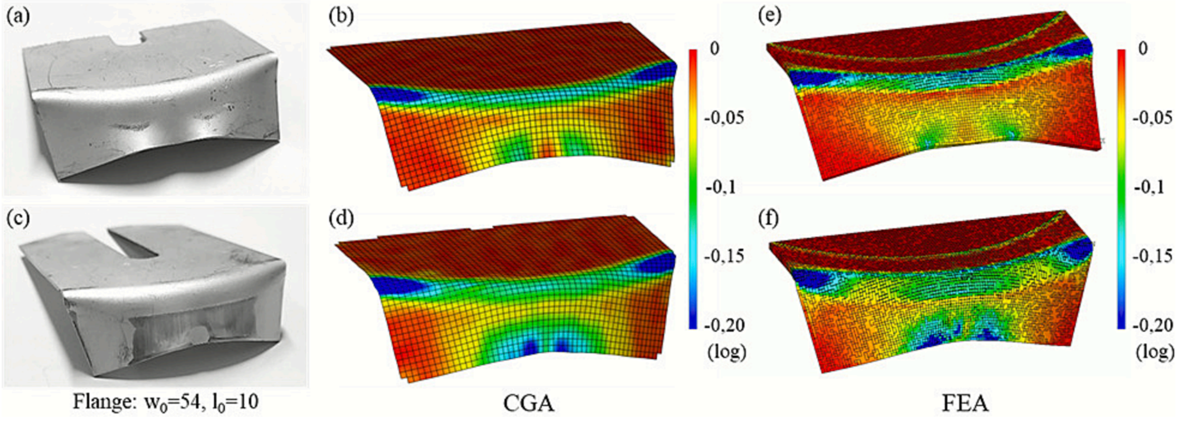

Fig. 16. Flanges of $w_0 = 54$ mm and $l_0 = 10$ mm obtained by CPF. (a) and (c) corresponds to the isometric view of the flange specimens before the ironing process and after the ironing, respectively. (b) and (d) represent the minor strain contours evaluated on the inner surface obtained using CGA for those flanges. (e) and (f) represent the minor strain contours evaluated on the inner surface obtained using FEA for those flanges.

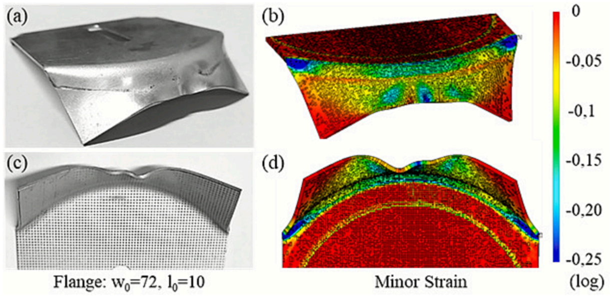

Fig. 17. Flange of $w_0 = 72$ mm and $l_0 = 10$ mm obtained by CPF. (a) and (c) correspond to the isometric and bottom view of the flange specimen, respectively. (b) and (d) represent the minor strain contours evaluated on the inner surface obtained using FEA for those flanges.

is followed by a second segment with equal slope, during which the wrinkle develops until the beginning of the ironing process. In the third segment, ironing reduces the wrinkle curvature, and in the fourth segment, the sheet is compressed between the die and the punch.

Several conclusions can be drawn from the strain evolution at the critical points. Firstly, in order to obtain a flange without wrinkles, the strain path must remain constant throughout the process. Second, a change in the direction of the strain path, which can happen on one or both surfaces, inner and outer, is related to wrinkling. Third, during the ironing stage, the amplitude of the wrinkles is reduced, compressing them following a proportional strain reproducing what happens in flanges without wrinkles. Finally, no pattern was observed in the strain level at which wrinkles appear, likely due to the modification of boundary conditions related to the different values of w_0 and l_0, being impossible stablishing a wrinkling limit within the FLD.

A similar analysis within the FLD is shown in Fig. 19 for the three flanges obtained using SPIF, which corresponds to a successful flange of $w_0 = 54$ mm and $l_0 = 5$ mm (Fig. 19a), a successful flange of $w_0 = 54$ mm and $l_0 = 10$ mm (Fig. 19b), and a flange with incipient wrinkling of $w_0 = 45$ mm and $l_0 = 20$ mm (Fig. 19c). The curves represent the strain evolution on the outer and inner flange surfaces, respectively. As seen in Fig. 19a for the successful flange, the inner surface is in pure compression strain state, whereas the outer face experiences pure tension. This result is due to the effect of bending within the 3 mm fillet radius R_{fillet} in a very short flange, which causes tension on the outer surface and compression on the inner surface. For the wrinkle-free flange in Fig. 19b, the critical point is compressed on both surfaces, and the strain evolution mainly follows the pure compression line on both the inner and outer surfaces. Finally, the flange of Fig. 19c, which showed incipient wrinkling, has strains evolutions that coincide with pure compression on the inner surface and pure tension on the outer surface. This difference observed between the two surfaces is due to the flange deformation caused by incipient wrinkling.

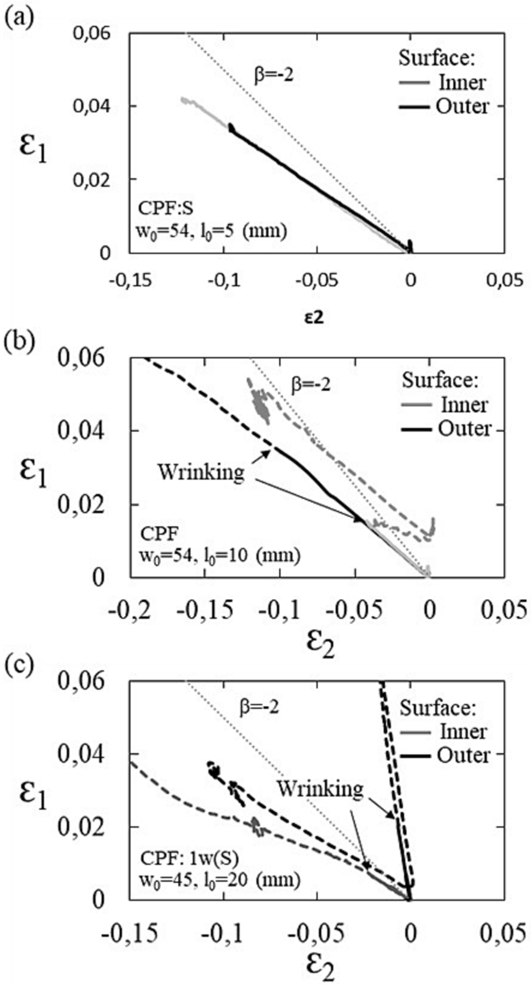

Fig. 18. Numerical evolution of principal strains at the critical point for three flanges manufactured using CPF evaluated on both surfaces of the sheet. (a) Flange without wrinkles. (b) Flange with two wrinkles. (c) flange with one wrinkle.

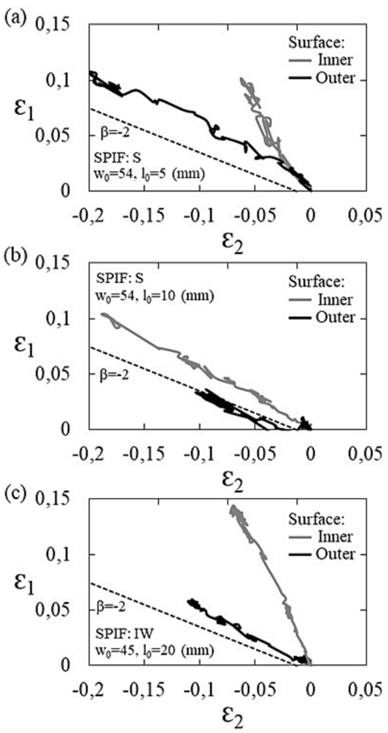

Fig. 19. Numerical evolution of principal strains at the critical point for three flanges manufactured using SPIF evaluated on both surfaces of the sheet. (a) and (b) correspond to successful flanges without wrinkles, and (c) corresponds to a flange with incipient wrinkling.

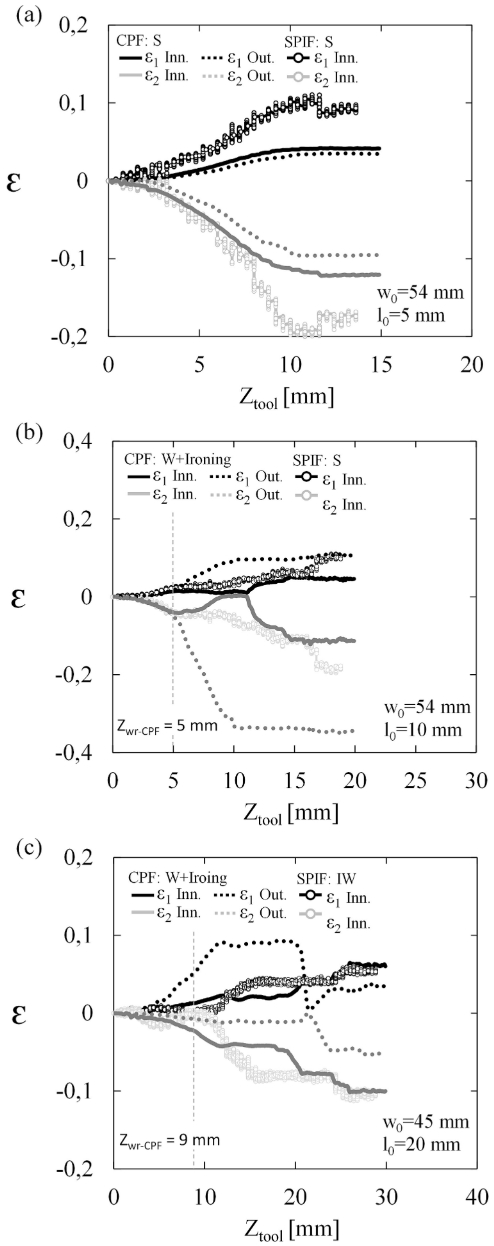

Fig. 20. Numerical evolution of principal strains at the critical point with respect to the tool displacement for flanges obtained using CPF and SPIF. (a) Flanges without wrinkles obtained by CPF and SPIF, respectively. (b) Flange with wrinkling and ironing obtained by CPF and successful flange obtained by SPIF. (c) Flange with wrinkling and ironing obtained by CPF and flange with incipient wrinkling obtained by SPIF. The onset of wrinkling for the flanges obtained by press forming is represented as z_{wr-CPF}.

Comparatively, some differences can be highlighted depending on the forming process used. On the one hand side, the compression strains reached before wrinkling are greater in SPIF, indicating increased formability in the incremental process. This can be observed by comparing the evolutions before wrinkling in Fig. 18 for flanges obtained using CPF with the strains in Fig. 19 for flanges without wrinkles obtained using SPIF. On the other hand, although wrinkling in flanges produced by CPF occurs at lower compression levels, the ironing phase produces compressions that reduces or removes the wrinkles that are of the same order or even greater than the compressions observed in SPIF. Finally, although the evolution in the FLD of several flanges with and without wrinkles has been shown, no clear pattern has been found to predict wrinkling. Therefore, the temporal evolution of principal strains for both processes will be analysed in what follows.

Fig. 20 shows the evolution over time of the minor and major strains on both surfaces of the flanges obtained using CPF analysed in Fig. 18. To compare both processes, the strain evolution of the inner surface of the flanges obtained by SPIF have been represented. In Fig. 20a, corresponding to a wrinkle-free flange, the evolution of the flange obtained by CPF is smooth on both the outer and the inner surfaces. Furthermore, due to the principal radius of the flange, the minor strain is lower on the inner surface than on the outer surface, whereas the major strain is quite similar on both surfaces. Additionally, the flange obtained using SPIF has higher major strain and lower minor strain levels, indicating more circumferential compression and radial stretching, respectively. On the other hand, the strain evolutions on both surfaces of the flange with wrinkling and ironing performed through CPF (Fig. 20b) are different. Concretely, at about 5 mm depth ($z_{wr\text{-}CPF.}$), the minor and major strain curves diverge due to the onset of wrinkling, which was calibrated experimentally for these specimens. As the process continues, the wrinkles are reduced through ironing, causing trend changes in the curves. In contrast, the flange produced through SPIF has a nearly linear strain evolution with no significant trend changes, as this flange does not have wrinkles. In this case, the compression levels corresponding to CPF are higher than those of the flange obtained through SPIF. Lastly, the flange with wrinkling and ironing represented in Fig. 20c also shows a separation of the strain curves corresponding to the two surfaces. In this case, wrinkling occurs at an approximate value of $z_{wr\text{-}CPF} = 9$ mm in depth in the opposite direction that in the previous case, resulting in higher compression on the inner surface. Additionally, the effect of ironing on the wrinkles causes several trend changes until reaching $z_{tool} = 30$ mm. Regarding the SPIF flange, the strain evolutions have slight trend changes corresponding to the appearance of incipient wrinkles which are consistent with its failure mode.

5.4. *Strain-based numerical criterion for the numerical assessment of wrinkling*

Based on the previous results, it can be said that wrinkles are characterised by greater deformation on one surface of the sheet than on the other. Similar strain-based and stress-driven approaches have also been applied to aluminium sheet forming by Shahzamanian et al. (2024). Based on this principle, it is possible to determine when a wrinkle has occurred by comparatively analysing the deformations on both surfaces of the flange at the critical wrinkling point, both in CPF and SPIF. Therefore, a criterion has been defined to detect wrinkling by analysing the deformation difference at the critical wrinkling point on the two surfaces of the sheet.

Firstly, it is necessary to consider that, after the forming process and neglecting the springback effect, the flange has a radius which equals the forming die radius. For this ideal case, the outer and the inner surfaces have a difference in the minor strains $\Delta\varepsilon_2$ which can be determined using Eq. (5). Where R_{out} and R_{in} are the outer and inner radii of the flange. Furthermore, considering the negligible thickness strain of the sheet, the radii of the two surfaces can be expressed in terms of the die radius R_{die} and the sheet thickness t.

$$\Delta\varepsilon_2 = \ln\left(\frac{R_{out}}{R_{in}}\right) = \ln\left(\frac{R_{die}+t}{R_{die}}\right) \tag{5}$$

Using Eq. (5) and introducing the values of the flanges analysed, $R_{die} = 45$ mm and $t = 1.2$ mm, the difference in minor strain due only to the flange curvature radius is $\Delta\varepsilon_{2,0} \approx 0.03$, as schematically represented in Fig. 21a. This value results directly from the flange geometry through Eq. (5) and is therefore applicable to any flange radius, with the value changing systematically with R_{die}. For illustration, using the same sheet thickness ($t = 1.2mm$), $\Delta\varepsilon_2, 0$ corresponds to approximately 0.04 for $R = 30$ mm and 0.02 for $R = 60mm$.

Therefore, on the theoretical basis, wrinkling occurs when $\Delta\varepsilon_2 > 0.03$, which is a conservative criterion considering that elastic recovery reduces the actual $\Delta\varepsilon_2$. However, before applying the methodology to evaluate the presence of wrinkles, it is necessary to consider that wrinkles can occur in both sheet directions. In this regards, two different cases may occur.

The first one is when the wrinkle centre of curvature is on the same side of the sheet as the flange radius, as shown in the diagram in Fig. 21b. In this case, $\Delta\varepsilon_2 = \varepsilon_{2,out} - \varepsilon_{2,in} > \varepsilon_{cir,0}$ where $\varepsilon_{2,out}$ and $\varepsilon_{2,in}$ are the strains at the analysed point on the outer and inner surface, respectively, and $\varepsilon_{cir,0}$ is the circumferential strain in the edge of the flange. For the flange radius and sheet thickness analysed, wrinkling occurs when the separation of the minor strain curves is $\Delta\varepsilon_2 > 0.03$. This case has been represented in Fig. 22a for the flange of $w_0 = 45$ mm and $l_0 = 20$ mm obtained by CPF (see Fig. 20c), where the black curve and the grey curve represent the minor strain evaluated on the outer and the inner surfaces, respectively, and the dashed line corresponds to the minor strain $\Delta\varepsilon_2$. For this flange, the onset of wrinkling, defined as z_{crit} occurs at $z_{tool} \approx 9mm$.

The second case is applied when the wrinkle occurs in the opposite direction and the outer surface is more compressed than the inner surface, and the sheet goes from $\Delta\varepsilon_2 = 0.03$ (Fig. 21a) to $\Delta\varepsilon_2 = 0$, corresponding to a straight flange as depicted in figure 21c. In the specific case $\Delta\varepsilon_2 = 0$, the minor strain curves $\varepsilon_{2,out}$ and $\varepsilon_{2,in}$ intersect, as represented in Fig. 22b for the flange of $w_0 = 54$ mm and $l_0 = 10$ mm analysed in Fig. 20b. Subsequently, if wrinkling goes on, the geometry of the flange becomes as represented in Fig. 21d for $\Delta\varepsilon_2 < 0$. In this context, it must be noted that the value of $\Delta\varepsilon_{cir,0}$ used to determine the onset of wrinkling has shown good accuracy in evaluating wrinkling in the analysed flanges. Furthermore, a slight variation in this value does not significantly change the wrinkling onset, $\Delta\varepsilon_2$ usually increases very rapidly, as shown in Fig. 22.

Although the proposed criterion for evaluating wrinkling can detect the initiation of a wrinkle, it cannot predict wrinkling. In this regard, it has not been possible to establish a wrinkle prediction criterion based on strains, which sets, for example, a common critical value for different flanges. To achieve this, Section 5.5 will conduct an analysis in terms of stresses, that uses the proposed criterion to determine the wrinkling onset, to then evaluate the critical stress value at that moment.

5.5. *Formability analysis for CPF and SPIF*

Considering that wrinkling is an instability influenced by the stress state and the boundary conditions, a set of flanges will be analysed in terms of stresses. In this section, the stress evolution of the critical points in flanges obtained using CPF and flanges performed by SPIF will be compared. Additionally, the critical stress values at wrinkling will be numerically obtained for a large number of flanges. Finally, the wrinkling limit will be determined in terms of stress for a wide set of flange widths and lengths.

5.5.1. *Analysis of wrinkling in terms of stresses*

It has been observed that, for the analysed flanges, principal strains analysis is insufficient to predict wrinkling. However, although the FE model has been shown to accurately reproduce the wrinkle topology observed in experiments, relying solely on this geometry for wrinkling detection would require manual inspection of each simulation case, which is impractical for extensive parametric studies. Defining a wrinkling criterion in terms of stress offers significant advantages in terms of automation and programmability, enabling the post-processing of large

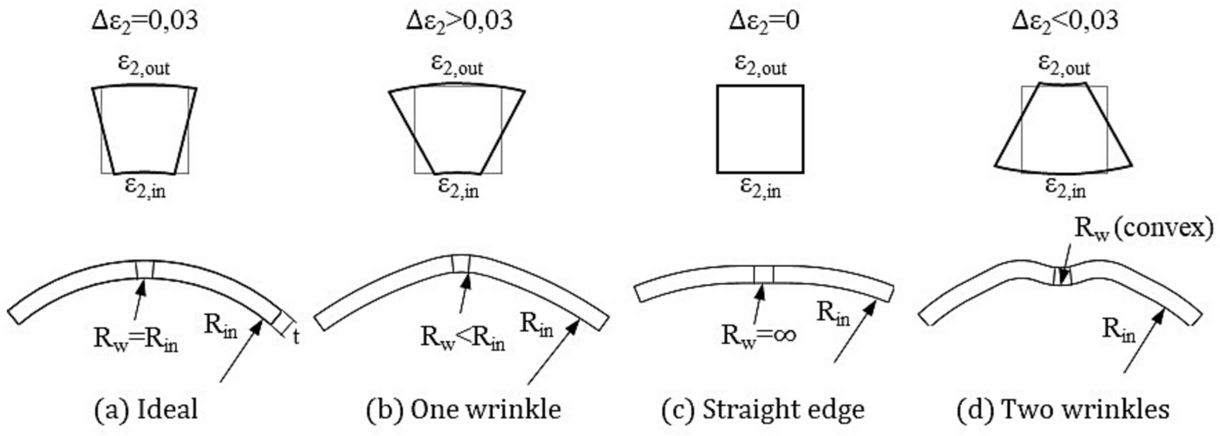

Fig. 21. Schematic representation of the edge profile for the following cases: (a) The ideal edge profile of a flange, (b) the profile of a flange with one wrinkle, (c) the profile of a flange with two wrinkles at the onset of wrinkling, and (d) the profile of a flange with two wrinkles after wrinkling.

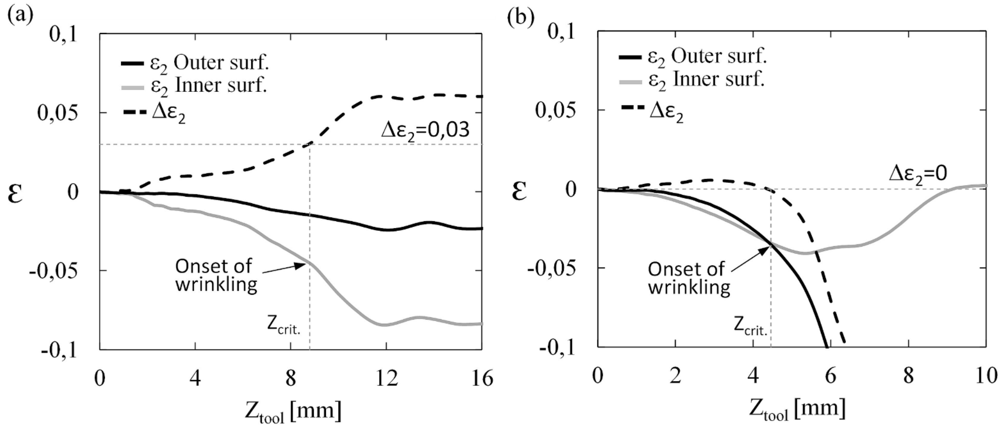

Fig. 22. Wrinkling detection criterion applied to two flanges. (a) A flange of $w_0 = 45$ mm and $l_0 = 20$ mm obtained by CPF with one wrinkle at the centre. (b) A flange of $w_0 = 54$ mm and $l_0 = 10$ mm with two wrinkles.

sets of simulations to identify wrinkling onset efficiently. Consequently, the flanges will be studied in terms of stresses. To this end, the in-plane stresses at the critical point have been simulated numerically for the tests contained in Table 5.

Fig. 23 shows the evolution of stresses at the critical wrinkling point for three flanges obtained through CPF and SPIF, respectively. The flanges selected correspond to those analysed in terms of principal strains in sections 5.2 and 5.3. For the flanges obtained using CPF, the analysis focuses on the evolution of major and minor stress in the plane of the sheet for the outer and inner surfaces. Regarding the flanges obtained through SPIF, it has been demonstrated that the stress evolution fluctuates due to successive tool passes (López-Fernández et al., 2023). Consequently, the values of the local minimums of minor stress were studied, represented by the lower envelope of the compression stresses in the plane, which is the same approach used in this study. These envelopes were evaluated on the inner surface, as this is the most compressed surface.

Fig. 23a illustrates the stress evolution for successful flanges with $w_0 = 54$ mm and $l_0 = 5$ mm. For the flange obtained using CPF, the major and minor stress evolutions on both surfaces are smooth until reaching $z_{tool} = 10$ mm, which marks the point at which the tool reached the critical point. Despite the absence of wrinkles in this flange (see Fig. 20a), a change in the stress curve from the inner and outer surfaces is observed as a result of the ironing process. With regard to the major stress σ_1 in the plane of the sheet, it is nearly zero until the ironing at $z_{tool} = 10$ mm, when it becomes negative. It is important to note that σ_1 and σ_2 are the principal stresses in the plane of the sheet and it is possible for σ_1 to be negative if the through-thickness stress is positive. Regarding the minor stress σ_2, the curves of both surfaces are very similar, and reach a minimum of -400 MPa. In the case of SPIF, the minor stress is lower than in CPF, indicating that the incremental process produces higher compression in the flange. Fig. 23a depicts the wrinkling limit in terms of compression stress for SPIF represented as a dotted line with $\sigma_2 = -530$ MPa (López-Fernández et al., 2023). This value is lower than the compressive stress measured in the analysed flange, as the flange was successful.

The behaviour of the flanges with wrinkling will be analysed through the results shown in Fig. 23b and 23c. The flanges analysed in Fig. 23b, with $w_0 = 54$ mm and $l_0 = 10$ mm, correspond to a flange with two wrinkles obtained in CPF and a flange without wrinkles obtained through SPIF. In the first case, the stress evolution on both surfaces shows no trend changes until $z_{tool} = 5$ mm. At this point, the curves of the outer and inner surfaces diverge, indicating a difference in the stress state on both surfaces at $z_{tool} = 5$ mm that marks the onset of wrinkling. From this point onwards, the curves exhibit inflection points corresponding to wrinkle compression between the die and the punch. Finally, when the flange is completely formed, the stresses on both surfaces are equal. In this flange, the curves diverge in $z_{tool} = 5$ mm at $\sigma_2 = -370$ MPa. This point coincides with the onset of wrinkling for this flange evaluated using the methodology presented in section 5.3, as shown in Fig. 22b. With regard to the successful flange formed by SPIF, the minor stress envelope is below the critical wrinkling value evaluated for the CPF flange ($\sigma_2 = -370$ MPa), indicating an increased formability of SPIF.

However, the selection of the wrinkling point in conventional forming based on the observation of the stress curves can not be applied to all flanges, as the stresses do not always diverge at the onset of wrinkling. An example of this will be described in Fig. 23c, which corresponds to a flange with one wrinkle. Consequently, it is necessary to apply the criterion for the evaluation of wrinkling based on strains in order to detect the onset of wrinkling, which can be applied to all cases, and subsequently the wrinkling stress at that moment. The analysis presented in Fig. 23c corresponds to a flange with $w_0 = 45$ mm and $l_0 = 20$ mm. When formed through CPF, this flange has two wrinkles, whereas the same flange formed by SPIF shows incipient wrinkling. In this case, the stress curves for CPF on both surfaces are very similar up to $z_{tool} = 20$ mm. However, in both stress components, the curves show several trend changes that are small for $z_{tool} < 10$ mm but larger for $z_{tool} > 10$ mm. This case demonstrates that the wrinkling onset is not always easily determined by analysing the stress evolution. By applying the wrinkling detection method previously described, it was determined that the first wrinkle initiates at $z_{tool} = 9$ mm, as shown in Fig. 22b, which corresponds to $\sigma_2 = -355$ MPa. The flange obtained using SPIF again has lower σ_2 stress than the flange formed using CPF. This is consistent with an increase of formability, as the wrinkles of this flange using SPIF appeared at $z_{tool} = 23$ mm and $\sigma_2 = -530$ MPa, and confirms the limited of σ_2 for wrinkling previously defined (López-Fernández et al., 2023). Although $\Delta\varepsilon_2$ and σ_2 may be expected to be physically related (since they both characterise aspects of the local deformation state) the boundary conditions in the present flanging processes, which depend strongly on w_0 and l_0, make it difficult to establish a general analytical or empirical correlation across all tested geometries.

The previous stress analysis has demonstrated that the stress values in flanges obtained using CPF vary compared to those obtained using SPIF. On the one hand, it has been shown that the SPIF process increases formability, delaying or eliminating wrinkling. In this regard, it has been observed that in SPIF, it is possible to reach significantly lower σ_2 values than in CPF without wrinkling. On the other hand, it has been demonstrated that the comparison of stresses on both surfaces of the flange is an ineffective method for detecting wrinkling, whereas the strain-based method outlined in section 5.4 is a more effective approach. Consequently, the optimal method for determining the wrinkling stress in a

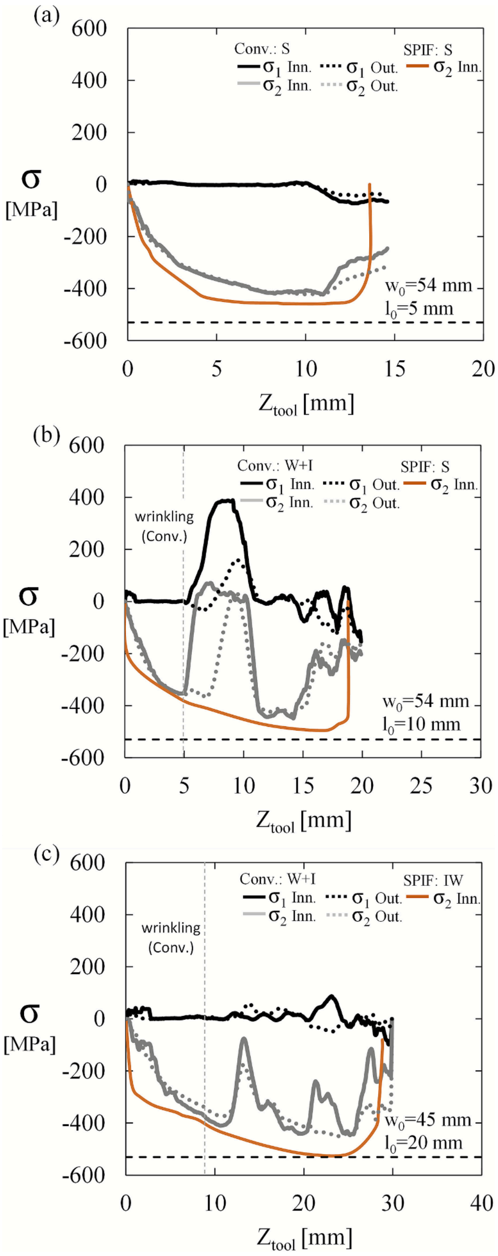

Fig. 23. Numerical evolution of principal stresses at the critical point with respect to the tool displacement for flanges obtained using CPF and SPIF. (a) Successful flanges obtained by CPF and SPIF. (b) Flange with wrinkling and ironing obtained by CPF and successful flange obtained by SPIF. (c) Flange with wrinkling and ironing obtained by CPF and flange with incipient wrinkling obtained by SPIF.

flange involves two steps. Initially, the onset of wrinkling is determined based on the separation of the deformation curves. Then, the wrinkling stress of the flange at the wrinkling moment, designated as $\sigma_{2,w}$, is obtained.

5.5.2. *Comparison of wrinkling limits for CPF and SPIF*

The aforementioned methodology has been employed to obtain the critical wrinkling stress values $\sigma_{2,w}$ for flanges with different w_0 and l_0. Fig. 24 presents the wrinkling stress values corresponding to all the flanges contained in Table 5. Furthermore, the figure includes an additional set of flanges with intermediate w_0 and l_0 values, thereby reducing the potential for interpolation errors. Each series represents a flange width w_0, while the initial length is shown on the horizontal axis. Upon examination of the various series, it is significant that the series of points obtained for different w_0 are remarkably similar, which indicates that the wrinkling stress is consistent across different flange widths. However, a clear trend is observed in the relationship between flange length and wrinkling stress. Specifically, it arises that the wrinkling stress is lower for shorter flanges than for longer flanges. This flange behaviour is represented by a regression curve that includes all the critical wrinkling values for the flanges under analysis, which corresponds to the wrinkling limit for these flanges. Additionally, it has been found that flanges with $l_0 < 7.5$ mm do not present wrinkles, resulting in a vertical limit between 5 mm and 7.5 mm. Considering these limits, Fig. 24 represents the global wrinkling process window for flanges with $R = 45$ mm, where the area labelled “successful” represents the compression stress values that can be achieved using CPF without wrinkling.

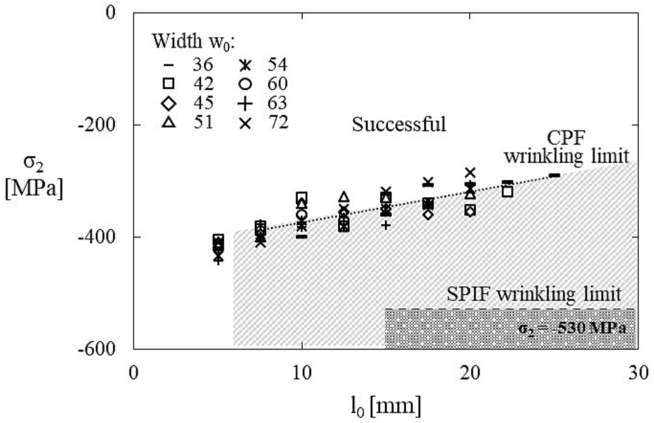

Fig. 24. Critical values of wrinkling stress for different shrink flanges of flange radius $R = 45$ mm obtained by Conventional Press Forming and by Single Point Incremental Forming, respectively.

Previous analyses (López-Fernández et al., 2023) demonstrated that the critical wrinkling stress remains almost constant for flanges obtained using SPIF. Specifically, for flanges with $R = 45$ mm, a wrinkling limit of $\sigma_2 = -530$ MPa was obtained, which is represented in Fig. 24 using a dashed line. Additionally, as occurred for the flanges obtained using CPF, there is a value of l_0 below which no wrinkles occur. In this case, the limit is represented in Fig. 24 between $l_0 = 10$ mm and $l_0 = 15$ mm. A comparison of the wrinkling limit obtained in SPIF with the limit in CPF indicates that the SPIF process allows reaching lower σ_2 values for all values of l_0 and w_0 analysed. This result aligns with those shown in Table 3, which indicate greater formability in SPIF.

In summary, the results demonstrate that the wrinkling conditions depend on the forming process. Generally speaking, in CPF, the wrinkling stress depends mainly on the length l_0, while in SPIF, the critical stress value seems to remain constant for different values of w_0 and l_0. Nevertheless, although wrinkling occurs at lower compression in CPF, it is possible to eliminate or reduce the number of wrinkles by ironing, thereby producing flanges that have high quality from an industrial perspective. Therefore, the selection of the appropriate process should not be based only on the wrinkling stress but should also consider whether a wrinkled flange obtained through CPF can be successfully ironed.

6. Conclusions

This article analyses comprehensively two different flange forming processes: The conventional press forming (CPF) process, which is widely used in the aerospace and automotive industries, and the single point incremental forming (SPIF) process, which is less studied but increasingly implemented, are the focus of this study. The first part of this study summarises and reviews the latest research on compression flange forming using both conventional and incremental processes and examines recent discoveries in flange wrinkling, aiding future researchers in obtaining the latest conclusions in this field. The rest of the article compares CPF and SPIF through the study of flanges with a radius of R = 45 mm, which represents a medium flange size in the aerospace industry. Several conclusions have been drawn from the analysis conducted.

The primary contribution of this study is the classification of the failure modes and the obtaining of the process windows. It has been demonstrated that flanges fail in different ways depending on the forming process selected and the flange geometry. In CPF, the flanges always wrinkle, except for very small l_0 values. These wrinkles result in two distinct behaviours: (i) wrinkling followed by ironing, which refers to flanges with wrinkles that can be reduced by a compression between the die and the tool, and (ii) wrinkling followed by fracture, which refers to flanges with wrinkles that are too large to be compressed and lead to fracture. Two failure modes were observed for flanges obtained via SPIF: wrinkling, corresponding to flanges with obvious wrinkles, and incipient wrinkling, referring to flanges with a polygonal shape due to local buckling that do not develop full wrinkles. In addition to these differences in wrinkling behaviour, CPF and SPIF also show distinct thickness change patterns: CPF ironing tends to increase edge thickening, whereas SPIF produces a more uniform thickness profile but with greater overall thinning.

This is the first time that an experimental campaign has been conducted to obtain the process windows for CPF and SPIF simultaneously for a wide range of flange widths and lengths. The results demonstrated that a significant proportion of flanges exhibited wrinkling when formed by CPF, but not when formed by SPIF. However, many of the CPF flanges with wrinkles could subsequently be ironed to produce flanges of higher quality than their SPIF counterparts. This study presents a process window that helps for the selection of the appropriate process based not only on the feasibility of manufacturing the flange but also on the geometric quality.

The second contribution of this work is the understanding and prediction of wrinkling in flanges. Flange deformation was quantified using Circle Grid Analysis (CGA), the critical points where wrinkling occurs were identified and the strain distribution in SPIF and CPF were critically compared. Based on the results, it has not been possible to predict wrinkling for either SPIF or CPF using the principal strain diagram, as use to be done in fracture.

Two finite element models have been used to predict the onset of wrinkling for both forming processes. Furthermore, the study of temporal stress evolution, in conjunction with the wrinkling detection methodology, allowed the determination of the in-plane minor stress values that cause wrinkling for a large set of flanges with different geometries. As the FE models reproduced the wrinkle topology with good agreement to experiments, defining a wrinkling limit in terms of stress provides an efficient and automatable tool for wrinkling assessment, particularly useful for extensive parametric analyses. This analysis has demonstrated that the critical wrinkling values in CPF are dependent on the flange length l_0 and are independent of the flange width w_0. Moreover, the value of compression stress at wrinkling for CPF is always lower than in SPIF, indicating that the formability in CPF is lower. In this context, the diagram created using the critical wrinkling values represents the process windows that allows the prediction of wrinkling for flanges with R = 45 mm for SPIF and CPF. This diagram reveals a wider wrinkle-free forming zone in SPIF.

Finally, although the wrinkling limits for CPF and SPIF have been determined, it is important to note that the results correspond to a specific flange radius, which is R = 45 mm. Therefore, it is possible that these values vary for different radii. From the authors' perspective, further work must be accomplished to analyse flanges of different radii. In addition, establishing a wrinkling limit in terms of stress for the specific boundary conditions of this study can serve as a first step toward automated parametric studies in problems with similar process setups. However, additional work is required to evaluate the applicability of the observed limits to forming conditions different from those investigated in this. Furthermore, this article has focused on formability analysis, whereas a detailed assessment of final shape and surface quality was not conducted. In this regard, future work is needed to perform a comparative analysis of both processes in terms of accuracy and surface finishing.

CRediT authorship contribution statement

J.A. López-Fernández: Writing – original draft, Software, Methodology, Investigation, Formal analysis, Conceptualization. **G. Centeno:** Writing – review & editing, Supervision, Methodology, Investigation, Funding acquisition, Conceptualization. **M.B. Silva:** Writing – review & editing, Supervision, Investigation, Funding acquisition, Conceptualization. **C. Vallellano:** Writing – review & editing, Supervision, Methodology, Investigation, Funding acquisition, Conceptualization.

Declaration of competing interest

The authors declare that they have no known competing financial interests or personal relationships that could have appeared to influence the work reported in this paper.

Acknowledgements

The authors acknowledge the funding provided by Grant PID2021-125934OB-I00 financed by MCIN/AEI/10.13039/501100011033 and by ERDF “A way of making Europe” (EU), the Grant TED2021-131153B-C22 funded by MICIU/AEI/10.13039/501100011033 and by the European Union under NextGenerationEU/PRTR, The Universty of Málaga through its "Funding for open access charge: Universidad de Málaga / CBUA", and M.B. Silva acknowledge Fundação para a Ciência e a Tecnologia (FCT) for its financial support via the project LAETA Base Funding (DOI:10.54499/UIDB/50022/2020).

Data availability

Data will be made available on request.

References

Dewang, Y., Sharma, V., 2023. Sheet metal shrink flanging process: a critical review of current scenario and future prospects. Mater. Manuf. Process. 38 (6), 629–658. https://doi.org/10.1080/10426914.2022.2149779.

Bałon, P., Rejman, E., Kiełbasa, B., Smusz, R., Szostak, J., Cieślik, J., 2019. A process of forming austenitic steel using a rubber membrane and oil, in AIP Conference Proceedings, American Institute of Physics Inc., 10.1063/1.5112639.

Tao, R., et al., 2023. Research on wrinkling in rubber forming of the convex flange with 2A12 aluminum alloy sheet, J. Adv. Mech. Desig. Syst. Manuf., 17(2), doi: 10.1299/jamdsm.2023jamdsm0016.

Sun, Y.N., Wan, M., Wu, X.D., 2013. Wrinkling prediction in rubber forming of Ti-15-3 alloy. Trans. Nonferrous Met. Soc. China (English Ed.) 23 (10), 3002–3010. https://doi.org/10.1016/S1003-6326(13)62827-7.

Chen, L., Chen, H., Wu, C., Tong, S., 2016. Experimental and numerical studies on the formability of TB5 titanium sheet in rubber cold forming. Int. J. Adv. Manuf. Technol. 86 (5–8), 2255–2264. https://doi.org/10.1007/s00170-016-8366-1.

Asnafi, 1999. On stretch and shrink flanging of sheet aluminium by fluid forming, J. Mater Process. Technol., 96.

Wang, X., Cao, J., Li, M., 2001. Wrinkling analysis in shrink flanging. J. Manuf. Sci. E. T. ASME 123 (3), 426–432. https://doi.org/10.1115/1.1381397.

Sinke, J., 2012. Forming limits for shrink flanges of rubber formed parts. Key Eng. Mater. 1255–1260. https://doi.org/10.4028/www.scientific.net/KEM.504-506.1255. Trans Tech Publications Ltd.

Chen, L., 2011. Numerical simulation and die compensation on springback of shrink flanging in rubber forming. In: Proceedings - 3rd International Conference on Measuring Technology and Mechatronics Automation, ICMTMA, pp. 705–708. https://doi.org/10.1109/ICMTMA.2011.460.

Chen, L., Chen, H., Wang, Q., Li, Z., 2015. Studies on wrinkling and control method in rubber forming using aluminium sheet shrink flanging process. Mater. Des. 65, 505–510. https://doi.org/10.1016/j.matdes.2014.09.057.

Chen, L., Bai, Y., Jiang, Z., Chen, H., Wu, C., Wang, Q., 2019. Numerical and experimental studies on wrinkling control methods of sheet metal part with high curvature and large flange in rubber forming. Adv. Mech. Eng. 11 (10). https://doi.org/10.1177/1687814019883787.

Wang, C.-T., Tufekci, S., Kinzel, G.L., Altan, T., 1994. Investigation of shrink flanging-prediction of wrinkling and experimental verification.

Hu, P., Li, D.Y., Li, Y.X., 2003. Analytical models of stretch and shrink flanging. Int. J. Mach. Tool Manuf. 43 (13), 1367–1373. https://doi.org/10.1016/S0890-6955(03)00150-0.

Zhang, G.E., Yao, J., Hu, S.J., Wu, X., 2003. Shrink flanging with surface contours. J. Manuf. Process. 5 (2), 143–153. https://doi.org/10.1016/s1526-6125(03)70049-8.

Draghici, C., 2017. Feasibilty analysis of shrink flanging process with support of numerical simulation, U.P.B. Sci. Bull., Series D, 79.

Horton, P.M., Allwood, J.M., Cleaver, C., Nagy-Sochacki, A., 2020. An experimental analysis of the relationship between the corner, die and punch radii in forming isolated flanged shrink corners from Al 5251. J. Mater. Process. Technol. 278. https://doi.org/10.1016/j.jmatprotec.2019.116486.

Emmens, W.C., Sebastiani, G., van den Boogaard, A.H., Jun. 2010. The technology of Incremental Sheet Forming-a brief review of the history. J. Mater. Process. Technol. 210 (8), 981–997. https://doi.org/10.1016/j.jmatprotec.2010.02.014.

Leszak, E., 1964. US 3,342,051; Apparatus and process for incremental dieless forming.

Harfoush, A., Fan, Z., Haapala, K.R., 2024. Experimental studies on multistage single point incremental forming of thin high carbon steel sheet. Int. J. Adv. Manuf. Technol. 132 (11–12), 5585–5596. https://doi.org/10.1007/s00170-024-13712-7.

Thakur, S., Chauhan, S.R., 2024. Development of a critical edge-based adaptive toolpath strategy to improve geometrical accuracy of incrementally formed titanium implants. J. Manuf. Process. 110, 114–125. https://doi.org/10.1016/j.jmapro.2023.12.053.

Choudhary, S., Mulay, A., 2024. Influence of tool size and step depth on the formability behavior of AA1050, AA6061-T6, and AA7075-T6 by single-point incremental forming process. J. Mater. Eng. Perform. 33 (7), 3283–3298. https://doi.org/10.1007/s11665-023-08231-7.

Bishnoi, P., Chandna, P., 2024. Optimizing the SPIF parameters for enhancing microhardness and surface quality in Inconel 625 superalloy components. J. Alloy. Compd. 997. https://doi.org/10.1016/j.jallcom.2024.174839.

Tayebi, P., Hashemi, R., 2024. Study of single point incremental forming limits of Al 1050/Mg-AZ31B two-layer sheets fabricated by roll bonding technique: finite element simulation and experiment. J. Mater. Res. Technol. 29, 149–169. https://doi.org/10.1016/j.jmrt.2024.01.085.

Zhu, H., Ou, H., Popov, A., 2020. Incremental sheet forming of thermoplastics: a review. Int. J. Adv. Manuf. Technol. 111 (1–2), 565–587. https://doi.org/10.1007/s00170-020-06056-5.

Rosa-Sainz, A., Centeno Báez, G., Silva, M.B., Vallellano, C., 2023. On the assessment of the failure strains in conventional and incremental forming of polymer sheets, Key Eng. Mater., 957, 41–50, 10.4028/p-1ljolN.

Emami, R., Mirnia, M.J., Elyasi, M., Zolfaghari, A., 2023. An experimental investigation into single point incremental forming of glass fiber-reinforced polyamide sheet with different fiber orientations and volume fractions at elevated temperatures. J. Thermoplast. Compos. Mater. 36 (5), 1893–1917. https://doi.org/10.1177/08927057221074266.

Borrego, M., Morales-Palma, D., Martínez-Donaire, A.J., Centeno, G., Vallellano, C., 2016. Experimental study of hole-flanging by single-stage incremental sheet forming. J. Mater. Process. Technol. 237, 320–330. https://doi.org/10.1016/j.jmatprotec.2016.06.026.

Mezher, M.T., Mustafa Khazaal, S., Namer, N.S.M., Shakir, R.A., 2021. A comparative analysis study of hole flanging by incremental sheet forming process of AA1060 and DC01 sheet metals.

Praveen, K.G., Kurra, S., 2021. Analysis of deformation behavior in various incremental tube forming processes. Mater. Manuf. Process. 36 (14), 1631–1641. https://doi.org/10.1080/10426914.2021.1926493.

Cristino, V.A., Magrinho, J.P., Centeno, G., Silva, M.B., Martins, P.A.F., 2021. Theory of single point incremental forming of tubes. J. Mater. Process. Technol. 287. https://doi.org/10.1016/j.jmatprotec.2020.116659.

Suntaxi, C., Centeno, G., Silva, M.B., Vallellano, C., Martins, P.A.F., 2021. Tube expansion by single point incremental forming: an experimental and numerical investigation. Metals (basel) 11 (9). https://doi.org/10.3390/met11091481.

Powell, N.N., Andrew, C., 1992. Incremental forming of flanged sheet metal components without dedicated dies. Proc. Inst. Mech. Eng. 206, 41–47.

López-Fernández, J.A., Borrego, M., Centeno, G., Vallellano, C., 2024. Fracture in stretch flanging by single point incremental forming. Int. J. Mech. Sci. 278. https://doi.org/10.1016/j.ijmecsci.2024.109438.

Gohil, A., Modi, B., 2021. Review of the effect of process parameters on performance measures in the incremental sheet forming process, SAGE Publications Ltd. doi: 10.1177/0954405420961215.

Chen, X., Wen, T., Hu, J., Zhang, M., Fang, J., 2019. Investigation of factors affecting the formability of metallic sheets in dieless incremental hole-flanging. Int. J. Adv. Manuf. Technol. 103 (5–8), 2609–2620. https://doi.org/10.1007/s00170-019-03459-x.

Basak, S., et al., 2020. Parameter optimization and texture evolution in single point incremental sheet forming process. Proc. Inst. Mech. Eng. B J. Eng. Manuf. 234 (1–2), 126–139. https://doi.org/10.1177/0954405419846001.

Ullah, S., Xu, P., Li, X., Li, Y., Han, K., Li, D., 2022. A review on part geometric precision improvement strategies in double-sided incremental forming, MDPI. doi: 10.3390/met12010103.

Wang, Y., Wang, L., Zhang, H., Gu, Y., Ye, Y., 2022. A novel algorithm for thickness prediction in incremental sheet metal forming, Materials, 15(3), doi: 10.3390/ma15031201.

Choi, H., Lee, C., 2019. A mathematical model to predict thickness distribution and formability of incremental forming combined with stretch forming. Rob. Comput. Integr. Manuf. 55, 164–172. https://doi.org/10.1016/j.rcim.2018.07.014.

Guzmán, C.F., Gu, J., Duflou, J., Vanhove, H., Flores, P., Habraken, A.M., 2012. Study of the geometrical inaccuracy on a SPIF two-slope pyramid by finite element simulations. Int. J. Solids Struct. 3594–3604. https://doi.org/10.1016/j.ijsolstr.2012.07.016.

Voswinckel, H., Bambach, M., Hirt, G., 2015. Improving geometrical accuracy for flanging by incremental sheet metal forming. Int. J. Mater. Form. 8 (3), 391–399. https://doi.org/10.1007/s12289-014-1182-y.

Ostasevicius, V., Paleviciute, I., Paulauskaite-taraseviciene, A., Jurenas, V., Eidukynas, D., Kizauskiene, L., 2022. Comparative analysis of machine learning methods for predicting robotized incremental metal sheet forming force, Sensors, 22(1), 10.3390/s22010018.

Guzmán, C.F., Yuan, S., Duchêne, L., Saavedra Flores, E.I., Habraken, A.M., 2018. Damage prediction in single point incremental forming using an extended Gurson model, Int. J. Solids Struct., 151, 45–56, doi: 10.1016/j.ijsolstr.2017.04.013.

Hamedon, Z., Abe, Y., Mori, K., 2016. Improvement of formability of high strength steel sheets in shrink flanging. IOP Conf. Ser.: Mater. Sci. Eng. https://doi.org/10.1088/1757-899X/114/1/012001. Institute of Physics Publishing.

Seyyedi, S.E., Gorji, H., Bakhshi-Jooybari, M., Mirnia, M.J., 2023. Comparison between conventional press-working and incremental forming in hole-flanging of AA6061-T6 sheets using a ductile fracture model. Int. J. Solids Struct. 270, 112225. https://doi.org/10.1016/j.ijsolstr.2023.112225.

Voswinckel, H., Bambach, M., Hirt, G., 2013. Process limits of stretch and shrink flanging by incremental sheet metal forming. Key Eng. Mater. 45–52. https://doi.org/10.4028/www.scientific.net/KEM.549.45. Trans Tech Publications Ltd.

Zhang, H., Zhang, Z., Ren, H., Cao, J., Chen, J., 2018. Deformation mechanics and failure mode in stretch and shrink flanging by double-sided incremental forming. Int. J. Mech. Sci. 144, 216–222. https://doi.org/10.1016/j.ijmecsci.2018.06.002.

Chen, S.W., Zhan, M., Gao, P.F., Ma, F., Zhang, H.R., 2021. A new robust theoretical prediction model for flange wrinkling in conventional spinning. J. Mater. Process. Technol. 288. https://doi.org/10.1016/j.jmatprotec.2020.116849.

López-Fernández, J.A., Centeno, G., Vallellano, C., 2023. Wrinkling in shrink flanging by single point incremental forming. Int. J. Mech. Sci. 240. https://doi.org/10.1016/j.ijmecsci.2022.107930.

Annison, R., Becque, J., 2025. A mechanics-based design approach to local buckling of thin-walled cross-sections. Int. J. Solids Struct. 319. https://doi.org/10.1016/j.ijsolstr.2025.113487.

Vallellano, C., Morales, D., García-Lomas, F.J., 2008. A study to predict failure in biaxially stretched sheets of aluminum alloy 2024-T3. Mater. Manuf. Process. 23 (3), 303–310. https://doi.org/10.1080/10426910801974804.

ASTM, Standard Test Methods for Tension Testing of Metallic Materials 1, 2009. doi: 10.1520/E0008_E0008M-09.

ASTM, "E517-00 Standard Test Method for Plastic Strain Ratio r for Sheet Metal," 2000. doi: 10.1520/E0517-00.

International Standard, 2021. ISO 12004-2:2021 Metallic materials — Determination of forming-limit curves for sheet and strip. Part 2: Determination of forming-limit curves in the laboratory., International Standard.

Martínez-Donaire, A.J., García-Lomas, F.J., Vallellano, C., 2014. New approaches to detect the onset of localised necking in sheets under through-thickness strain gradients. Mater. Des. 57, 135–145. https://doi.org/10.1016/j.matdes.2014.01.012.

López-Fernández, J.A., Centeno, G., Martínez-Donaire, A.J., Morales-Palma, D., Vallellano, C., 2019. Critical evaluation of the formability of AA2024-T3 sheet deformed by single-point incremental forming, Dyna (Medellin), 94(5), 10.6036/9141.

López-Fernández, J.A., Centeno, G., Martínez-Donaire, A.J., Morales-Palma, D., Vallellano, C., 2021. Stretch-flanging of AA2024-T3 sheet by single-stage SPIF, Thin-Walled Struct., 160(107338), doi: 10.1016/j.tws.2020.107338.

Centeno, G., Martínez-Donaire, A.J., Morales-Palma, D., Vallellano, C., Silva, M.B., Martins, P.A.F., 2015. Novel experimental techniques for the determination of the forming limits at necking and fracture, Mater. Forming Mach.: Res. Develop., 1–24, doi: 10.1016/B978-0-85709-483-4.00001-6.

Palomo, D., Martinez-Donaire, A.J., Lopez-Fernandez, J.A., Borrego, M., Vallellano, C., 2022. Preliminary study on the onset of necking detection using DIT in tensile tests, 926 KEM, doi: 10.4028/p-ad49jb.

Neto, D.M., Coër, J., Oliveira, M.C., Alves, J.L., Manach, P.Y., Menezes, L.F., 2016. Numerical analysis on the elastic deformation of the tools in sheet metal forming processes. Int. J. Solids Struct. 100–101, 270–285. https://doi.org/10.1016/j.ijsolstr.2016.08.023.

Barlat, F., Lian, J., 1989. Plastic behavior and stretchability of sheet metals. part h a yield function for orthotropic sheets under plane stress conditions. Int. J. Plast 5, 51–66.

Logan, W., Hosford, F., 1980. Upper-bound anisotropic yield locus calculations assuming (111) - pencil glide. Int. J. Mech. Sci. 22, 419–430. https://doi.org/10.1016/0020-7403(80)90011-9.

Zhang, M.H., Lu, B., Chen, J., Long, H., Ou, H., 2015. Selective element fission approach for fast FEM simulation of incremental sheet forming based on dual-mesh system. Int. J. Adv. Manuf. Technol. 78 (5–8), 1147–1160. https://doi.org/10.1007/s00170-014-6723-5.

Magrinho, J.P.G., Silva, C.M.A., Silva, M.B., Martins, P.A.F., 2018. Formability limits by wrinkling in sheet metal forming. Proc. Inst. Mech. Eng., Part L: J. Mater.: Desig. Appl. 232 (8), 681–692. https://doi.org/10.1177/1464420716642794.

Shahzamanian, M.M., Parsazadeh, M., Wu, P.D., 2024. Numerical and analytical analyses of the formability and fracture of AA7075-O aluminum sheets in hemispherical punch tests. Int. J. Solids Struct. 286–287. https://doi.org/10.1016/j.ijsolstr.2023.112558.